Spring 2010

DLA-LBG cross-correlation and basic properties of infrared galaxies in cosmological simulations

Tae Song Lee
University of Nevada Las Vegas

DLA-LBG CROSS-CORRELATION AND BASIC PROPERTIES OF INFRARED GALAXIES IN COSMOLOGICAL SIMULATIONS

by

Tae Song Lee

Bachelor of Science
California State University, Northridge
1998

Master of Science
University of Nevada, Las Vegas
2007

A dissertation submitted in partial fulfillment
of the requirements for the

Doctor of Philosophy Degree in Astronomy
Department of Physics and Astronomy
College of Sciences

Graduate College
University of Nevada, Las Vegas
May 2010

UNLV
UNIVERSITY OF NEVADA LAS VEGAS

THE GRADUATE COLLEGE

We recommend the dissertation prepared under our supervision by

Tae Song Lee

entitled

DLA-LBG Cross-correlation and Basic Properties of Infrared Galaxies in Cosmological Simulations

be accepted in partial fulfillment of the requirements for the degree of

Doctor of Philosophy in Astronomy
Physics and Astronomy

Kentaro Nagamine, Committee Chair

Bing Zhang, Committee Member

Daniel Proga, Committee Member

Balakrishnan Naduvalath, Graduate Faculty Representative

Ronald Smith, Ph. D., Vice President for Research and Graduate Studies
and Dean of the Graduate College

May 2010

ABSTRACT

DLA-LBG Cross-correlation and Basic Properties of Infrared Galaxies in Cosmological Simulations

by

Tae Song Lee

Dr. Kentaro Nagamine, Examination Committee Chair
Assistant Professor of Astronomy
University of Nevada, Las Vegas

PART I

We calculate the cross-correlation function (CCF) between damped Ly-α systems (DLAs) and Lyman break galaxies (LBGs) using cosmological hydrodynamic simulations at $z = 3$. We compute the CCF with two different methods. First, we assume that there is one DLA in each dark matter halo if its DLA cross section is non-zero. In our second approach we weight the pair-count by the DLA cross section of each halo, yielding a cross-section-weighted CCF. We also compute the angular CCF for direct comparison with observations. Finally, we calculate the auto-correlation functions of LBGs and DLAs, and their bias against the dark matter distribution. For these different approaches, we consistently find that there is good agreement between our simulations and observational measurements by Cooke et al. (2006a) and Adelberger et al. (2005). Our results thus confirm that the spatial distribution of LBGs and DLAs can be well described within the framework of the concordance ΛCDM model. We find that the correlation strengths of LBGs and DLAs are consistent with the actual observations, and in the case of LBGs it is higher than would be predicted by low-mass galaxy merger models.

PARTII

We present theoretical computational results of magnitudes, luminosity functions, galaxy number counts, and redshift distribution in the 3.6, 4.5, 5.8, and 8.0 μms of IRAC and 24, 70, and 160 μms of MIPS bands using cosmological hydrodynamic simulations. We combine GADGET-3 with GRASIL spectrophotometic code to compute galaxy spectral energy distribution. We compare our luminosity function (IRAC: 8μm and MIPS: 24μm) results with observational and sampling data (Caputi et al., 2007; Rodighiero et al., 2009) from the *Spitzer Space Telescope*. We find that there is reliable agreement with their results.

TABLE OF CONTENTS

LIST OF TABLES

LIST OF FIGURES

ACKNOWLEDGMENTS

I would like to thank my advisor Dr. Kentaro Nagamine for his guidance and support. I would also like to thank my committee members Dr. Zhang and Dr. Proga. I thank Mr. John Kilburg for the computer support and the help that he gave.

Finally, loving thanks to my father (In-Su Lee), mother (Kinam Lee), sister (Kyongmi-Yuna Lee), and brother (Tae Yong Lee) who gave me great mental support. Specially, I owe my loving thanks to my dearest love, SoonAe who cares about me the most and is giving great encouragement. Without their support and understanding it wouldn't have been possible to finish this work.

CHAPTER 1

INTRODUCTION

ΛCDM is denoted as the standard model of big bang cosmology. This model makes an effort to explain the existence and structure of the large structure of galaxy clusters, cosmic microwave background (CMB), amount of hydrogen, helium, and the expansion of the universe observed with the light from Type Ia supernova and distant galaxies.

ΛCDM model incorporates an expansion of space that is mesured with the redshift of spectral lines in the light from distant galaxies and with the cosmological time dilation in the light degradation of supernovae (SN). The model is described under an assumption of flat universe that space is defined by straight lines. The current values of parameters indicate that the universe is expanding and accelerating. The key parameters from Wilkinson Microwave Anisotropy Probe (WMAP) are summaried in Table 1.

Parameters	Valuses	Description
t_0	13.75 ± 0.13 Gyr	Age of Universe
h	0.72	Hubble Constant
Ω_m	0.26	Dark Matter Density
Ω_b	0.044	Baryon Density
Ω_Λ	0.74	Dark Energy Density
n_x	0.96	Spectral Index
σ_8	0.80	Fluctuation amplitude at 8 h^{-1} Mpc

Table 1 WMAP Parameters

Cold dark matter (CDM) is a invisible matter required to answer for gravitational influences observed in large scale structures (e.g. the rotation velocity of galaxies

and the gravitational lensing of light by galaxy clusters) that cannot be explained by the amount of visible baryonic matters (protons and neutrons). Dark matter is characterized as being non-relativistic in its velocity and non-baryonic. It cannot be cooled by radiative processes and collisionless. The dark matters interact with each other and other particles via gravity only.

ΛCDM model includes the cosmological constant which is linked to a dark energy (Ω_Λ) inherent in a vacuum space. The dark energy describes the accelerating expansion of space in opposition to the attractive force of gravity by the baryonic and non-baryonic matters. The cosmological constant is interpreted as the fraction of the total mass density of a flat universe. The current measured value of Ω_Λ is stated in Table 1.

The Big Bang cosmology with a cosmic inflation which is included in ΛCDM model uses the Friedmann equations and cosmological equations of state to describe the observed universe from the inflation epoch to present time and currently ΛCDM model has been made the great successes and good agreements with the observations.

We made two theoretical approaches to explain the observations using the Smooth Particle Hydrodynamic (SPH) Cosmological Simulations. First, according to the cold dark matter (CDM) model of structure formation, the spatial distribution of galaxies can be understood as a result of gravitational instability of density fluctuations in the CDM, and the dark matter halo mass function can be well described by analytic models (Sheth & Tormen, 1999). More precisely, hierarchical CDM models predict that the massive galaxies at high redshift (hereafter high-z) are clustered together in high-density regions, while low-mass galaxies tend to be more evenly spaced (Kaiser, 1984; Bardeen et al., 1986). Under the assumption that galaxies are produced from primordial density fluctuations owing to gravitational instability, one can estimate the average mass of galaxy host haloes based on clustering data. Second, it is well

understood that massive galaxies have experienced a large portion of their star formation (SF) at early epoch. Understanding the infrared emission from dust is very important for theoretical predictions on when and how galaxies form. Deep surveys (e.g. *Infrared Space Observatory* and *Spitzer Space Telescope*) probe SF rate (SFR) in the distant galaxies with mid-infrared light. The evolution of the IR luminosity function has been measured up to z$\sim$ 2.5 (Caputi et al., 2007; Rodighiero et al., 2009).

CHAPTER 2

PART I: INTRODUCTION

Damped Lyman-α systems (DLAs), defined as quasar absorption systems with column density of $N_{\rm HI} > 2 \times 10^{20}$ atoms cm^{-2} (Wolfe et al., 1986), probe the H I gas associated with high-z galaxies. Since stars are hardly formed in warm ionized gas and are tightly correlated with cold neutral clouds, the amount of H I gas is very important, being the precursor of molecular clouds (Wolfe et al., 2003). DLAs dominate the H I content of the Universe at $z \simeq 3$ and contain a sufficient amount of H I gas mass to account for a large fraction of the present-day stellar mass (Storrie-Lombardi & Wolfe, 2000). The gas kinematics and chemical abundances of DLAs can be measured and are documented in detail. However, the masses of DLA host haloes (hereafter DLA haloes) remain poorly constrained, because only about 20% of quasars exhibit DLA absorption per unit redshift (Nagamine et al., 2007), and the scattered distribution of DLAs in quasar sight lines precludes the use of DLAs as tracers of dark matter halo mass.

Alternatively, the mass of DLA haloes can be probed by the cross-correlation between DLAs and a galaxy population whose clustering and halo mass are well understood. Cooke et al. (2006a,b) used 211 LBG spectra and 11 DLAs to measure the three dimensional (3-D) LBG ACF and DLA-LBG CCF (see also Gawiser et al., 2001; Bouche & Lowenthal, 2004; Bouche et al., 2005). Their analysis started by counting the number of LBGs in 3-D cylindrical bins centred on each of 11 DLAs, following the method of Adelberger et al. (2003). They estimated the typical halo mass of LBGs at $z \sim 3$ to be $10^{10.8} M_{\odot} \leq M_{\rm halo} \leq 10^{12}\, M_{\odot}$ from observations of their auto-correlation function (ACF) and detected a statistically significant result of DLA-LBG CCF, and estimated an average DLA halo mass of $\langle M_{\rm DLA} \rangle \approx 10^{11.2} M_{\odot}$, assuming a single galaxy per halo.

On the theoretical side, Nagamine et al. (2007) calculated the average DLA halo mass using a series of cosmological hydrodynamic simulations with different box sizes, resolution and feedback strengths. They found a mean DLA halo mass of $\langle M_{\rm DLA} \rangle = 10^{12.4} M_\odot$ with their Q5 run which is somewhat larger than $\langle M_{\rm DLA} \rangle = 10^{11.2} M_\odot$ of Cooke et al. (2006a). More recent work by Pontzen et al. (2008) showed that the DLA cross-section is predominantly provided by intermediate mass haloes, $10^9 < M_{\rm vir}/M_\odot < 10^{11}$. These results motivate us to further examine the distribution of DLAs relative to that of LBGs. In this paper, we compute the DLA-LBG CCF in cosmological SPH simulations, using the sample of LBGs and DLAs obtained by Nagamine et al. (2004a,b). We compare our results with the observational results by Adelberger et al. (2005) and Cooke et al. (2006a,b).

The part I is organized as follows. In Section 3, we briefly describe the features of our cosmological SPH simulations used in this paper. In Section 4 and Section 5, we describe and report the methodology, binning method, and the results for 'unweighted' and 'weighted' DLA-LBG CCF, respectively. We then discuss the projected angular CCF for the direct comparison with observational result by Cooke et al. (2006a,b) in Section 6. The ACFs of LBG-LBG and DLA-DLA are discussed in Subsections 7 and 7, while the bias results are reported in Section 8. Finally, we discuss the implications of our work in Section 9.

CHAPTER 3

SIMULATION

In the part I, we use two different cosmological smoothed particle hydrodynamics (SPH) simulations (Springel & Hernquist, 2003a) performed with the GADGET-2 code (Springel, 2005). The simulation parameters of the two runs (named D5 and G5) are summarized in Table 2. The same set of runs has been used by Nagamine et al. (2004b,a, 2007) to study the global properties of DLAs, such as the DLA cross section, incidence rate, and H I column density distribution functions.

The code we use is characterized by four main features. First, it uses an entropy-conserving formulation of SPH (Springel & Hernquist, 2002), which explicitly conserves entropy of the gas where appropriate. Second, highly overdense gas particles are treated with a sub-resolution model for the interstellar medium (ISM) (Springel & Hernquist, 2003b). The dense ISM is assumed to be made of a two-phase fluid consisting of cold clouds in pressure equilibrium with a hot ambient phase. Cold clouds grow by radiative cooling, and form the reservoir of baryons for star formation. Once star formation occurs, the resulting supernovae (SNe) deposit energy into the ISM, heating the hot gas environment, evaporating cold clouds, and transferring cold gas back into the ambient phase. This establishes a self-regulation cycle for star formation in the ISM, Additionally, the simulation keeps track of metal abundance and the dynamical transport of metals. Metals are produced by stars and returned into the gas by SNe.

Third, a model for galactic winds is included to study the effects of outflows on DLAs, galaxies, and intergalactic medium (IGM). In this model, gas particles are driven out of dense star-forming medium by assigning an extra momentum in random directions (Springel & Hernquist, 2003b). It is assumed that the wind mass-loss rate is proportional to the star formation rate, and the wind takes a fixed fraction of the

SN energy. For the D5 and G5 runs, a strong wind speed of $484\,\mathrm{km\,s^{-1}}$ is adopted (as opposed to the 'weak' wind speed of $242\,\mathrm{km\,s^{-1}}$; Springel & Hernquist (2003b)). The dependence of the wind models on DLA properties was discussed in detail by Nagamine et al. (2007). Fourth, the code includes radiative cooling and heating with a uniform UV background of a modified Haardt & Madau (1996) spectrum (Katz et al., 1996; Davé et al., 1999), where the reionisation takes place at $z \simeq 6$.

We identify galaxies in our simulation by grouping the star particles. We then calculate the luminosity and spectrum of individual star particles using the mass, formation time, and metallicity. The spectrum of each galaxy is obtained by coadding the spectrum of constituent star particles, and the broad-band colours are computed by convolving with filter functions. The LBGs are then selected based on the U_nGR colour selection criteria as described in Nagamine et al. (2004).

In the part II, we utilize three different SPH simulations carried out under GADGET-3 (Springel, 2005). GADGET-3 is the updated version of the smoothed particle hydrodynamics (SPH) code GADGET-2. A Tree-particle-mesh (TPM) algorithm is implemented to compute the gravitational dynamics. An SPH-TPM simulation allows a fast and reliable high-resolution calculation for gravitational and gaseous dynamics. The TPM algorithm is divided into two parts. For the long-range gravitational force, it uses a particle-mesh (PM) method by Hockney & Eastwood (1988), and the short-range gravitational force is computed by a tree method (Barnes & Hut, 1986). Advantages of using the TPM algorithm are: 1) the gravitational force calculation can be performed faster than the Tree method alone, and 2) in the dense regions, the TPM enables the higher force resolution than the PM method. The gas dynamics is computed by an SPH method. Especially, the SPH is advantageous when the simulation needs to deal with large dynamical extent such as the investigation of galaxy formation and evolution in a cosmological setting.

GADGET-3 uses an entropy-conserving formulation of SPH (Springel & Hernquist, 2002), which explicitly conserves entropy of the gas where appropriate. Highly over-dense gas particles, star formation, and supernova (SN) feedback are treated with a sub-resolution model for the interstellar medium (ISM) (Springel & Hernquist, 2003b). The dense ISM is assumed to be made of a two-phase fluid consisting of cold clouds in pressure equilibrium with a hot ambient phase. Cold clouds grow by radiative cooling, and form the reservoir of baryons for star formation. Once star formation occurs, the resulting supernovae (SNe) deposit energy into the ISM, heating the hot gas environment, increasing thermal energy of the hot gas, evaporating cold clouds, and transferring cold gas back into the ambient phase. The simulations incorporate radiative cooling and heating processes for hydrogen and helium using a method comparable to Katz et al. (1996). An external background radiation (ultraviolet) is considered as uniform photo-ionizing photons (Haardt & Madau, 1996). The normalization has been adjusted to be compatible with the Lyα forest observations (Davé et al., 1999). A single gas particle represents both hot and cold gas. The stars are formed in the cold portion when the density exceeds a given threshold, which is derived self-consistently within the sub-resolution model for the ISM. In addition to the sub-resolution model, a phenomenological model for SN-driven galactic wind (Springel & Hernquist, 2003a) is incorporated to the simulation. The galactic wind is particularly important for studying the effects of outflows on Damped Lyα Systems (DLAs), galaxies, and intergalactic medium (IGM), and for distributing the metals carried by SNe into the IGM. The strong kinematic wind with a speed of 484 kms^{-1} has been adopted. The previous works (Nagamine et al., 2004a,b) have shown that at z = 3 such model settings provide promising results for the luminosity function (LFs) of Lyman-break galaxies (LBGs) at the bright-end and for the HI column density distribution function, compared to the simulations without the galactic wind.

Run	$L_{\rm box}$	$N_{\rm p}$	$m_{\rm DM}$	$m_{\rm gas}$	ϵ
D5	33.75	2×324^3	8.15×10^7	1.26×10^7	4.17
G5	100.0	2×324^3	2.12×10^9	3.26×10^8	12.3

Table 2 Simulations employed in the part I. $N_{\rm P}$ is the initial number of gas and dark matter particles (hence $\times 2$). $m_{\rm DM}$ and $m_{\rm gas}$ are the masses of dark matter and gas particles in units of $h^{-1}M_{\odot}$, respectively. ϵ is the comoving gravitational softening length in units of $h^{-1}kpc$, which is a measure of spatial resolution. All runs adopt a strong galactic wind feedback model.

CHAPTER 4

DLA-LBG CROSS-CORRELATION

The probability of finding an object 1 in volume δV_1 at a separation r from a randomly chosen object 2 can be written as $\delta P = n_1 \left[1 + \xi_{12}(r)\right] \delta V_1$ (Peebles, 1980). The joint probability of finding an object 1 in volume 1 (δV_1) and an object 2 in volume 2 (δV_2) at a separation r is defined as $\delta P = n_1 n_2 \left[1 + \xi_{12}(r)\right] \delta V_1 \delta V_2$, where n_1 and n_2 are the mean number densities of the two population. For the cross-correlation, we replace object 1 and 2 with DLA and LBG, then the joint probability between DLA and LBG is

$$\delta P = n_{\rm DLA} n_{\rm LBG} \left[1 + \xi_{\rm DLA-LBG}(r)\right] \delta V_{\rm DLA} \delta V_{\rm LBG}, \tag{1}$$

where $n_{\rm DLA}$ and $n_{\rm LBG}$ are the mean number densities of DLAs and LBGs, and $\xi_{\rm DLA-LBG}(r)$ is the cross-correlation function (CCF).

To estimate $\xi_{\rm DLA-LBG}(r)$, we use the method of Landy & Szalay (1993) and Cooke et al. (2006a):

$$\xi_{\rm DLA-LBG}(r) = \frac{D_{\rm DLA} D_{\rm LBG} - D_{\rm DLA} R_{\rm LBG} - R_{\rm DLA} D_{\rm LBG} + R_{\rm DLA} R_{\rm LBG}}{R_{\rm DLA} R_{\rm LBG}}, \tag{2}$$

where $D_{\rm DLA} D_{\rm LBG}$ is the number of pairs between the two data samples of DLAs and LBGs separated by a distance $r \pm \delta r$, and likewise for other terms. The notation "$R_{\rm DLA}$", for example, represents the DLA sample that has random coordinate positions but with an equivalent number density as the original data sample "$D_{\rm DLA}$".

The method of identifying DLAs in our simulations is described in detail in Nagamine et al. (2004a) (See, also Katz et al. (1996a); Hernquist et al. (1996)). Briefly, we set up a cubic grid that completely covers each dark matter halo, with the grid-cell size equivalent to the gravitational softening length 'ϵ' of each run. We

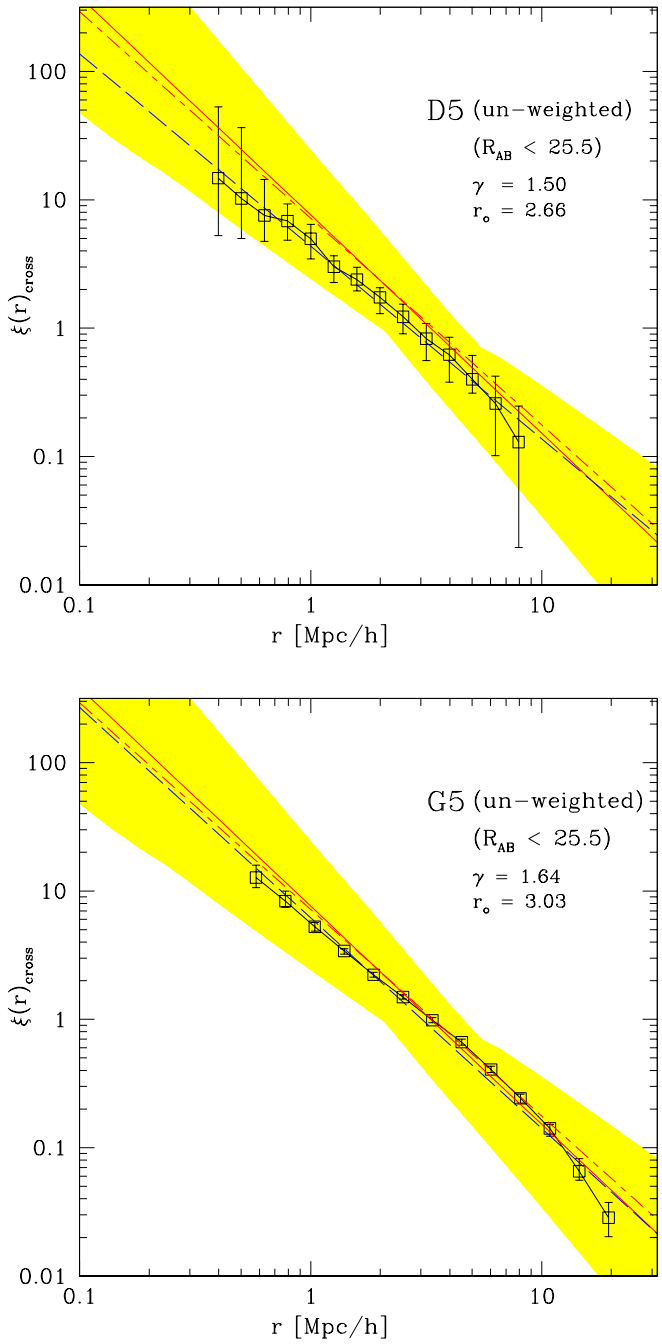

Figure 1 DLA-LBG CCFs at $z = 3$ calculated with the regular *unweighted* method (Equation 2). The variance of CCFs computed with 100 different random seeds is shown with vertical errorbars, and the open square symbols are the mean of 100 trials. The blue dashed line is the least-square fit to the open square points. The red solid line and the short and long dashed lines are the angular and 3-D best-fitting power-laws of Cooke et al. (2006a,b), respectively, and the yellow shade is their 1-σ error range for the angular CCF.

then calculate the H I column density $N_{\rm HI}$ of each pixel (i.e., a grid-cell on one of the planes) by projecting the H I mass distribution, and identify those that exceed the DLA threshold of $N_{HI} > 2 \times 10^{20}$ atoms cm^{-2} as 'DLA-pixels'. This method allows us to quantify the DLA cross-section '$\sigma_{\rm DLA}$' of each halo, and the number of DLA-pixel is $N_i^{\rm DLA} = \sigma_{\rm DLA}/\epsilon^2$. Here we focus on the correlation signal at $r \gtrsim 0.4\,h^{-1}\,$Mpc, because this is the scale probed by Cooke et al. (2006a,b). Therefore in this paper we are only concerned about the overall halo positions and not the exact locations of individual DLA-pixel within each halo. The $\sigma_{\rm DLA}$-weighted CCF will be discussed in Section 5.

First, we select the LBGs that are brighter than $R_{\rm AB}$=25.5 magnitude in the D5 and G5 runs. There are 30 (4030) LBGs in the D5 (G5) run. Nagamine et al. (2004) have shown that the brightest galaxies with $R_{\rm AB} < 25.5$ in our simulations satisfy the U_nGR colour selection criteria for LBGs (e.g., Steidel et al., 1999). Figure 2 of Nagamine et al. (2004) shows that the D5 run underestimates the number density of LBGs, while the G5 run agrees better with the observation.

There are 22616 (25683) DLA haloes with $\sigma_{\rm DLA} > 0$ in the simulated volumes of the D5 (G5) run. The 'random' catalogues of LBGs and DLA haloes with random positions were created with a random number generator from Numerical Recipes (Press et al., 1992). The selected LBGs were paired with DLA haloes, and the number of pairs that reside in spherical shells of $[\log r, \log r + \Delta \log r]$ were counted. The maximum pair separations probed for the D5 and G5 runs are 10 and $35\,h^{-1}\,$Mpc, respectively, with 20 bins in a logarithmic scale of distance r. The periodic boundary condition was taken into account appropriately, and the pair-search was extended to the next adjacent box where needed.

We correct all $\xi(r)$ values by the integral constraint (IC). This correction owes to the finite size of the observed field-of-view, and it must be added to the computed

	Unweighted		σ_{DLA}-weighted	
Run	r_0	γ	r_0	γ
D5	2.66 ± 0.23	1.50 ± 0.17	3.37 ± 0.36	1.77 ± 0.21
G5	3.03 ± 0.04	1.64 ± 0.03	3.43 ± 0.06	1.66 ± 0.03

Table 3 Best-fitting power-law parameters of unweighted and σ_{DLA}-weighted DLA-LBG CCFs at $z = 3$. The correlation length r_0 is in units of h^{-1}Mpc. The confidence limit statistics for this work are described in Section 5. For comparison, Cooke (private communication) obtained $r_0 = 2.91 \pm 1.0 h^{-1}$Mpc and $\gamma = 1.21^{+0.6}_{-0.3}$ for the 3-D CCF calculated with spherical shells, and Cooke et al. (2006b) reported $r_0 = 3.32 \pm 1.25 h^{-1}$Mpc and $\gamma = 1.74 \pm 0.36$ for the *angular* CCF.

correlation function as follows:

$$\xi'(r) = \xi(r) + \mathrm{IC}, \tag{3}$$

where $\xi'(r)$ and $\xi(r)$ are the corrected and computed CCF (or ACF) respectively. Following the method described in Adelberger et al. (2005) and Lee et al. (2006), we calculate the value of IC and find that it changes $\xi(r)$ only slightly in our simulations, with IC $\sim 10^{-2}$ for the D5 run.

Figure 1 shows the DLA-LBG CCF computed with Eq. (2). We perform a least-square fit to the measured values with a power-law $\xi(r) = (r_0/r)^\gamma$, and find best-fitting parameters equal to $(r_0[h^{-1}\,\mathrm{Mpc}], \gamma) = (2.66 \pm 0.23, 1.50 \pm 0.17)$ and $(3.03 \pm 0.04, 1.64 \pm 0.03)$ for the D5 and G5 runs, respectively. The fits are shown by the blue long-dashed lines (see also Table 3), and the confidence limit statistics are described in Section 5.

Landy & Szalay (1993) showed that the variance of $\omega_p(r_\theta)$ obtained from Monte Carlo calculations agrees quite well with the standard Poisson variance. Here, we follow their method outlined in their Section 5.2 and repeat the calculation of the CCF

100 times using different seeds for generating the random positions for the 'random' sample to examine the statistical variance of the measured CCF. The variance of 100 trials is shown as vertical errorbars, and the average of 100 trials is shown with the open square data points. The red solid line and the yellow shade represent the best-fitting result ($r_0 = 3.32 \pm 1.25$ and $\gamma = 1.74 \pm 0.36$) and the 1-σ errors of Cooke et al. (2006a,b) from their angular CCF result. The result of the G5 run agrees well with that of Cooke et al.'s, and its variance is small owing to a larger sample than in the D5 run. The result of the D5 run is somewhat shallower than that of the G5 run, which could simply owe to relatively small sample of LBGs in D5 and its small box-size.

Cooke et al. (2006a,b) published only the angular CCFs. However, they can also estimate the 3-D radial CCF using redshift information. The best-fitting parameters to the radial CCF by Cooke (private communication) using spherical shells is $r_0 = 3.39 \pm 1.2\,h^{-1}\,\mathrm{Mpc}$ and $\gamma = 1.61 \pm 0.3$, which is shallower than the angular CCF results. As we will further discuss in Section 6, the method of Adelberger et al. (2003) adopts cylindrical shells at small distances, which have larger volumes than spherical shells. The cylindrical shell method uses long cylinders at small r_θ and captures all the potential LBGs near the DLAs, whereas the spherical bins do not. This effect seems to result in the slightly steeper γ in Cooke et al. (2006b) compared to the above spherical shell case (Cooke; private communication). We regard the comparison to the angular CCF of Cooke et al. (2006b) as the primary one, because Cooke et al. argue that the angular CCF calculated by the method of Adelberger et al. (2003) is more robust than the 3-D radial calculation with spherical shells, and the values of (r_0, γ) derived from both CCFs should be equivalent theoretically (see Section 6).

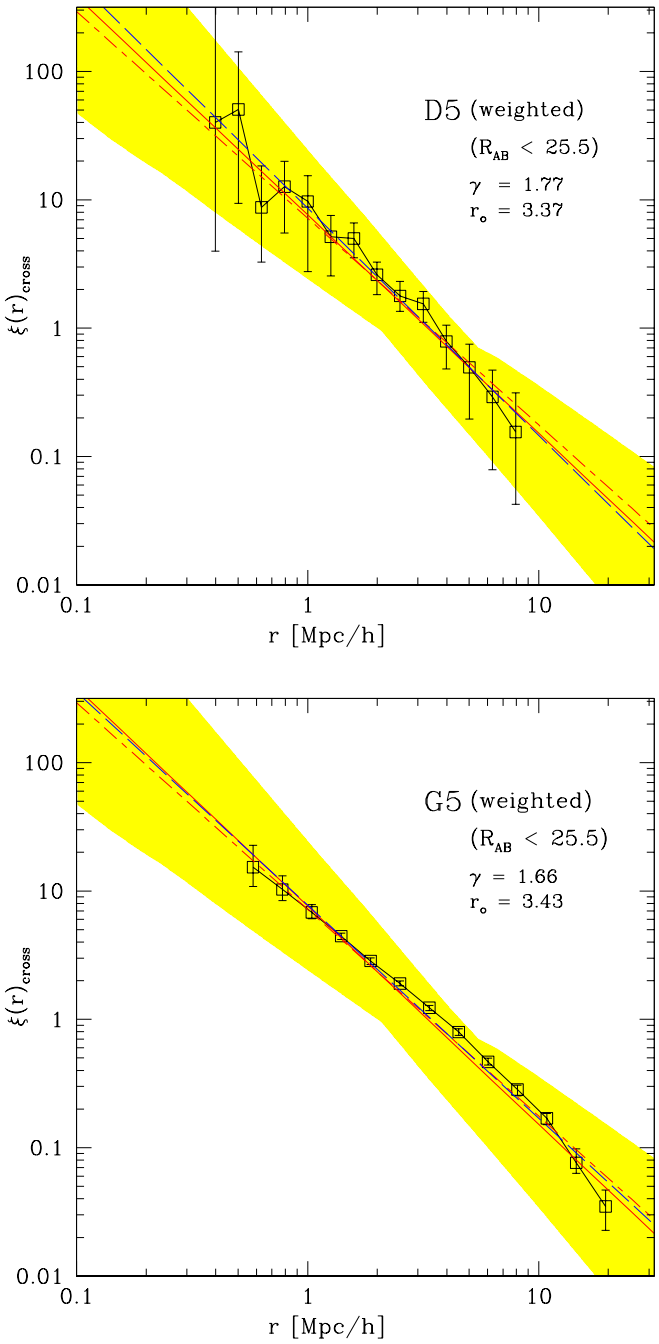

Figure 2 DLA-LBG CCF at $z = 3$ calculated by the $\sigma_{\rm DLA}$-weighted method (Equation 1). The yellow shade shows the upper and lower limits of Cooke et al. (2006a,b)'s best-fitting power-laws. The variance of the CCF using 100 random seeds shown with vertical errorbars. The blue dashed lines are the best-fittings for this work, and the red solid line and the short and long dashed lines are, respectively, the angular and 3-D best-fitting power-laws of Cooke et al. (2006a,b).

CHAPTER 5

$\sigma_{\rm DLA}$-WEIGHTED CCF

In Section 4, we calculated the CCF assuming that there is one DLA per halo. This assumption is valid as long as we are concerned with the CCF at scales of $r \gtrsim 300\,h^{-1}\,\mathrm{kpc}$. However, Nagamine et al. (2004b, Fig. 1) showed that the DLA clouds have extended distributions in massive dark matter haloes. Therefore, it may be more desirable to take the DLA cross-section of each halo into account when calculating the CCF, because the chance of finding a DLA in the actual observation is already cross-section weighted. Ideally, we would use all the DLA pixels and find pairs with the nearby LBGs, but this computation is prohibitively expensive owing to the large number of DLA pixels.

A simple way to achieve this is to weight the number of DLA-LBG pairs by the number of DLA-pixels of each halo. Since the displacement between DLA-pixels within a single halo is typically much smaller than the distance between LBG-DLA pairs, we do not count the individual pairs between LBG and DLA-pixels. Instead, we treat it as if all DLA-pixels are located at the halo centre, and weight each DLA-LBG pair-count by the number of DLA-pixels N_i (hereafter we drop the superscript 'DLA' for simplicity) and compute the $\sigma_{\rm DLA}$-weighted CCF as

$$\xi_{\rm DLA-LBG}(r) = \frac{N_i D_{\rm DLA} D_{\rm LBG} - N_i D_{\rm DLA} R_{\rm LBG} - N_i R_{\rm DLA} D_{\rm LBG} + N_i R_{\rm DLA} R_{\rm LBG}}{N_i R_{\rm DLA} R_{\rm LBG}}. \tag{1}$$

For the 'random' DLA dataset, we shuffle the original N_i list randomly and make new pairs with different DLA haloes. Again, 10 realisations of the random dataset have been used to examine the statistical variance of the estimated CCF.

The results for the $\sigma_{\rm DLA}$-weighted CCF is shown in Figure 2. We find best-fitting parameters of $(r_0\,[h^{-1}\,\mathrm{Mpc}], \gamma) = (3.37\pm0.36, 1.77\pm0.21)$ and $(3.43\pm0.06, 1.66\pm0.03)$

for the D5 and G5 runs, respectively, as shown by the blue long-dashed line (see also Table 3). (See Section 5 for the error estimates.) Both results show good agreement with the best-fitting values of Cooke et al. (2006b, $r_0 = 3.32 \pm 1.25$ and $\gamma = 1.74 \pm 0.36$). The result of D5 is somewhat noisy at $r \lesssim 1\,h^{-1}\,\mathrm{Mpc}$, which originates from the noisy pair-count of $N_i D_{\mathrm{DLA}} D_{\mathrm{LBG}}$.

The parameter values given in Table 3 clearly show that the σ_{DLA}-weighted method gives larger values of r_0 and a slightly steeper power-law slope. In a CDM universe, the number of low-mass haloes is far greater than that of massive haloes. Therefore, even a small weighting by N_i boosts up the overall pair-count, yielding a stronger correlation signal compared to the unweighted case. The larger LBG sample in the G5 run makes its result more robust against the weighting procedure than that of the D5 run. Therefore, the difference in the slope γ between the two calculation methods is smaller in the G5 run than that of D5 run.

Confidence Limits

The χ^2 test describes the goodness-of-fit of the model to the data. To determine the confidence intervals of the two parameters (γ and r_0), we use the minimum χ^2 method. This statistic is written as

$$\chi^2 \equiv \sum_{i=1}^{n} \frac{(O_i - E_i)^2}{\sigma_i^2}, \tag{2}$$

where O_i are the data points shown in the correlation figures, E_i are the expected values in each bin i from the power-law, and σ_i is the standard deviations in each bin obtained from the 100 Monte Carlo calculations, as described earlier.

The region of confidence limits (Avni, 1976) is given by

$$\chi_p^2 = \chi_{\mathrm{min}}^2 + \Delta(df, p), \tag{3}$$

where p is a confidence level ($0 < p < 1$), and df is a degree of freedom written as $df = n - c$, where n is the number of bins and c is the number of parameters. For this

work, $c = 2$ and $n = 13$ for G5 DLA-LBG CCFs (un-weighted and σ_{DLA}-weighted), G5 LBG-LBG ACF, and G5 DLA-DLA ACFs (un-weighted and σ_{DLA}-weighted); $n = 14$ for D5 DLA-LBG 3D and *angular* CCFs (un-weighted and σ_{DLA}-weighted); and $n = 17$ for G5 DLA-LBG *angular* CCFs (un-weighted and σ_{DLA}-weighted). The value $\Delta(df, p)$ is the expected increment of χ^2 to find the 68% and 95% confidence limits above $\chi^2_{\rm min}$. Its value is determined by the degree of freedom and probability within 1 and 2-σ limits. We calculate the 1-σ confidence limits for all the correlation cases using this method. As an example, we show the 1 and 2-σ confidence levels for the weighted CCFs of D5 and G5 runs in Figure 3.

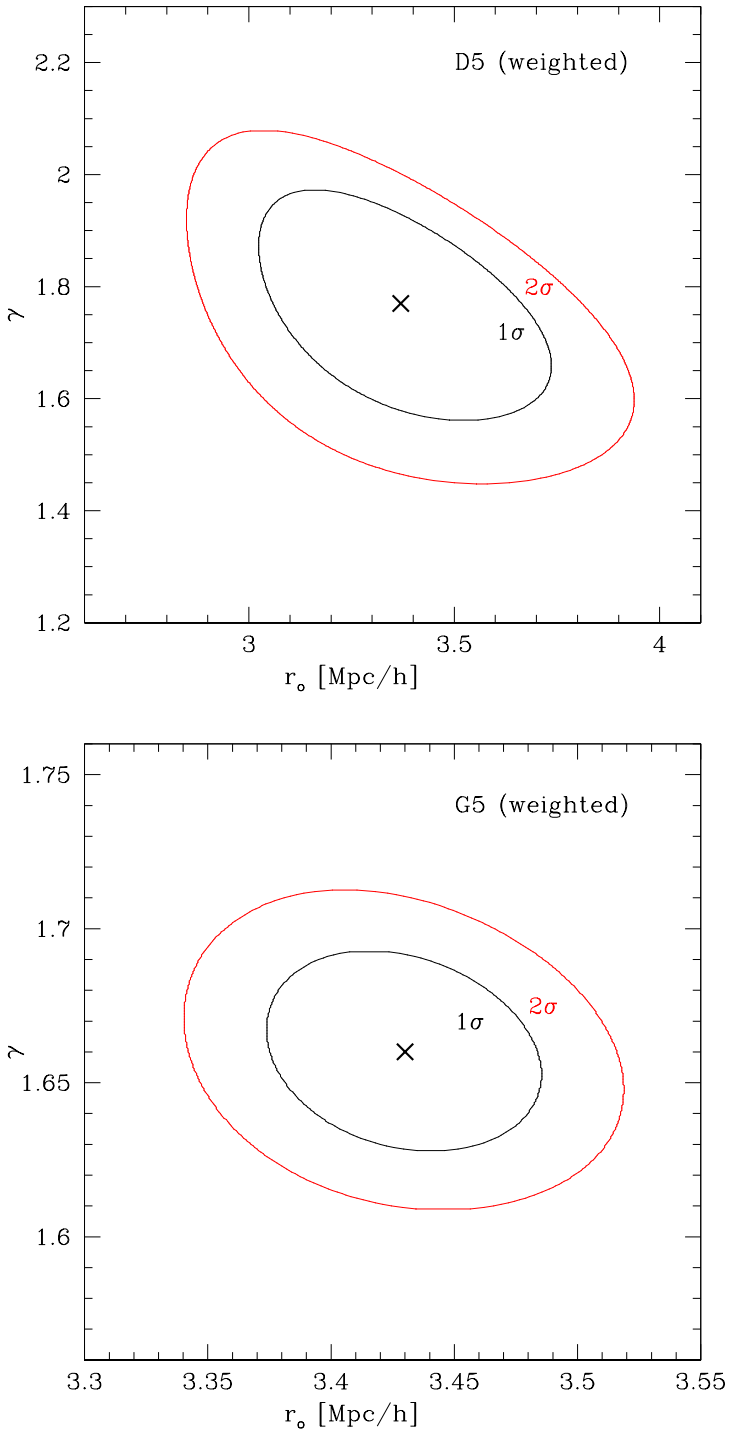

Figure 3 Two parameter confidence limit contours for the weighted DLA-LBG cross correlation case using the minimum χ^2 method. The best fits of the two parameters are indicated by the cross at the center of the contours, and 1 and 2-σ limits are shown in black and red contour lines, respectively.

CHAPTER 6

ANGULAR CROSS CORRELATION FUNCTION

In observational studies, a different method is usually used to obtain the values of (r_0, γ) compared with what we described in Sections 4 and 5, because the precise estimation of any LBG position along the line of sight is difficult to achieve owing to redshift uncertainties caused by peculiar velocities and galactic winds. With such imprecision, it is not possible to measure the CCF at scales $r \lesssim 1h^{-1}\,\mathrm{Mpc}$ reliably. Therefore, rather than attempting to estimate the 3-D distance between DLAs and LBGs, observers usually employ the angular CCF using the projected data on the sky. For example, Cooke et al. (2006a,b) computed the angular CCF using the method proposed by Adelberger et al. (2003). In order to compare our results with those by Cooke et al's, we briefly describe the calculation method of Adelberger et al. (2003), and then describe how we perform our measurement of the angular CCF.

With a power-law assumption, the expected number of pairs for the projected angular CCF is

$$\omega_p(r_\theta < r_z) = \frac{r_0^\gamma r_\theta^{1-\gamma}}{2r_z} B\left(\frac{1}{2}, \frac{\gamma-1}{2}\right) I_x\left(\frac{1}{2}, \frac{\gamma-1}{2}\right), \tag{1}$$

where B and I_x are the beta and incomplete beta functions with (e.g., Press et al., 1992)

$$x \equiv r_z^2 \left(r_z^2 + r_\theta^2\right)^{-1}. \tag{2}$$

Adelberger et al. (2003) proposed to count the number of pairs in cylindrical shells of angular separation $r_\theta \pm \delta r_\theta$ and redshift separation $r_z \pm \delta r_z$, rather than using spherical shells. By setting r_z to

$$r_z = \max\left(1000\ \mathrm{km\,s^{-1}} \frac{(1+zx)}{H(z)}, 7r_\theta\right), \tag{3}$$

the lower limit ensures that the redshift errors do not lead to the underestimate of

the number of pairs, and the upper limit allows sufficient distances to include enough correlated pairs (Adelberger et al., 2003).

For our calculations, we focus at $z = 3$ and thus $r_z = \max(12.8\,h^{-1}\,\mathrm{Mpc}, 7r_\theta)$. With simple algebra, Equation (1) can be converted to a more familiar power-law form:

$$\begin{aligned}\xi(r_\theta) &= 2r_{\max}\frac{\omega_p(r_\theta)}{r_\theta}\left[B\left(\frac{1}{2},\frac{\gamma-1}{2}\right)I_x\left(\frac{1}{2},\frac{\gamma-1}{2}\right)\right]^{-1} \\ &= \left(\frac{r_\theta}{r_0}\right)^{-\gamma}, \end{aligned} \tag{4}$$

where r_z is set to $r_{\max}$. We change from spherical coordinates to cylindrical coordinates, and set the number of cylindrical bins to 20 in a logarithmic scale as before. All pair searches are extended to the adjacent box using periodic boundary conditions, if appropriate.

A few assumptions must be made while we deal with the beta and incomplete beta functions. There are two parameters (γ and x) that must be given to calculate the values of B and I_x. To calculate γ, we first plot Equation (4) without B and I_x (i.e., $2r_{\max}\omega_p(r_\theta)/r_\theta$) and find the best-fitting value of γ. The value of x is determined by r_z and r_θ as shown in Equation (1). By setting $r_z = r_{\max}$, the angular separation will be divided into two different regimes. Within the smaller angular separation range ($100\,h^{-1}\,\mathrm{kpc} < r_\theta < 1.83\,h^{-1}\,\mathrm{Mpc}$), the correlated pairs are counted up to the maximum radial distance of $r_{\max} = \pm 12.8\,h^{-1}\,\mathrm{Mpc}$ for a cylinder centred on an LBG or DLA, while in the larger separation range ($r_\theta > 1.83\,h^{-1}\,\mathrm{Mpc}$) all the correlated pairs within $r_{\max} = \pm 7r_\theta$ are counted. We calculate the values of B and I_x (as well as the IC correction) separately for the two different r_θ regions. With the fixed values of γ obtained above and 20 different values of x, B and I_x can be calculated for each bin.

The angular CCF results of our calculations are shown in Figures 4 and 5 for

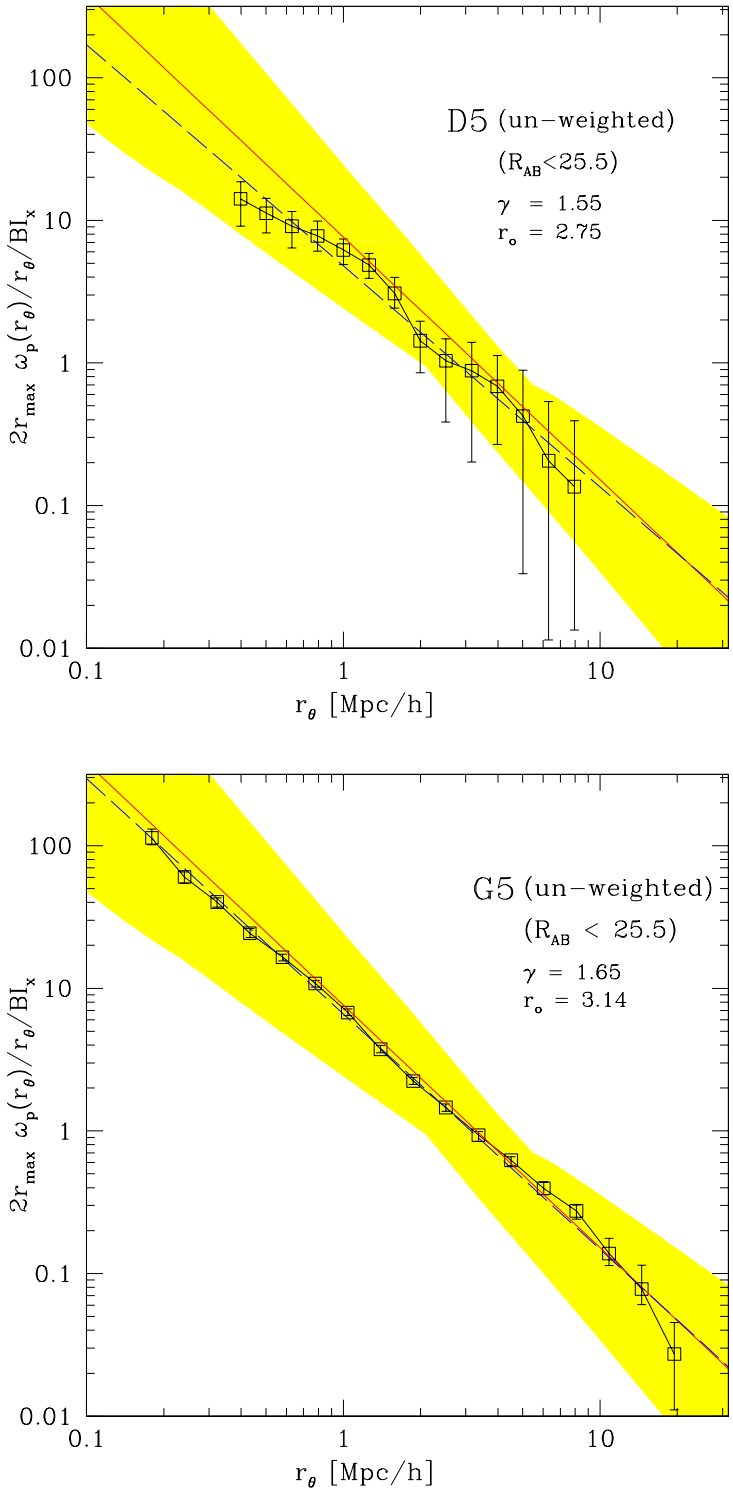

Figure 4 DLA-LBG *angular* CCFs at $z = 3$ computed by the *unweighted* method for the D5 and G5 runs. Other features are the same as described in Figure 1.

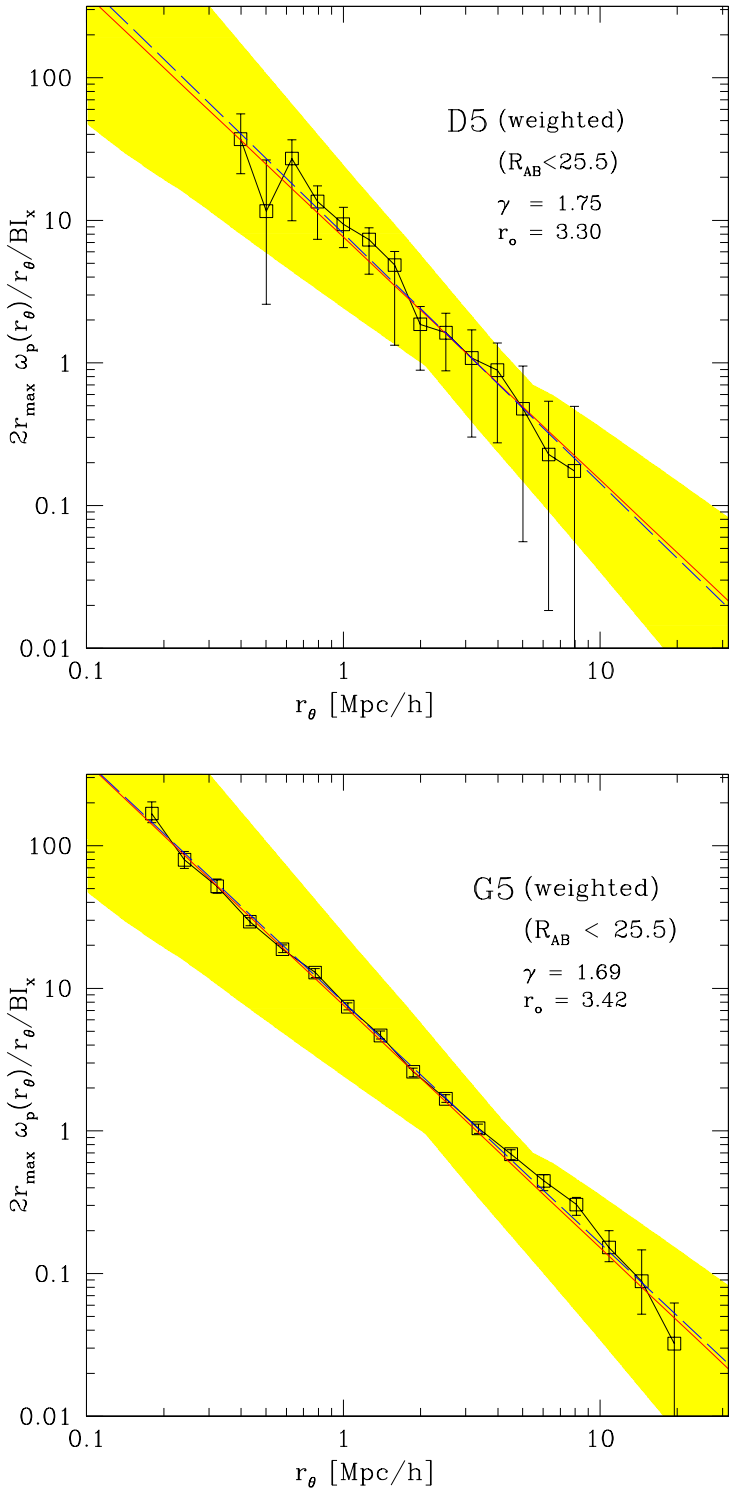

Figure 5 DLA-LBG *angular* CCFs at $z = 3$ computed by the $\sigma_{\rm DLA}$-weighted method for the D5 and G5 runs. Other features are the same as described in Figure 1.

	Unweighted		$\sigma_{\rm DLA}$-weighted	
Run	r_0	γ	r_0	γ
D5	2.75 ± 0.51	1.55 ± 0.20	3.30 ± 0.60	1.75 ± 0.23
G5	3.14 ± 0.28	1.65 ± 0.09	3.42 ± 0.32	1.69 ± 0.10

Table 4 Best-fitting power-law parameters for the *angular* CCF at $z = 3$. The units of the parameters are the same as in Table 3. The confidence limit statistics are described in Section 5. For comparison, Cooke et al. (2006b) reported $r_0 = 3.32 \pm 1.25\,h^{-1}$ Mpc and $\gamma = 1.74 \pm 0.36$ for their angular CCF.

both the unweighted and the $\sigma_{\rm DLA}$-weighted method. The best-fitting power-law parameters are given in Table 4. Again, the agreement with the results of Cooke et al. (2006a,b) is within a good range. Similarly to the 3-D CCF case, the $\sigma_{\rm DLA}$-weighted case gives a slightly larger r_0 and steeper γ than the unweighted case. The unweighted case of D5 is shallow with $\gamma = 1.55$, but in the $\sigma_{\rm DLA}$-weighted case, $\gamma \simeq 1.75$ is recovered.

CHAPTER 7

AUTO-CORRELATION FUNCTIONS

LBG auto-correlation

The auto-correlation function (ACF) also gives important constraints on the distribution of the population under study. In this section, we calculate the 3-D LBG ACF by changing all subscripts in Equation (2) to 'LBG':

$$\xi_{\rm LBG-LBG}(r) = \frac{D_{\rm LBG}D_{\rm LBG} - 2D_{\rm LBG}R_{\rm LBG} + R_{\rm LBG}D_{\rm LBG}}{R_{\rm LBG}R_{\rm LBG}}. \quad (1)$$

Our result for the ACF is shown in Figure 6, and the best-fitting power-law parameters (see Section 5 for confidence limit statistics) are $r_0 = 3.86 \pm 0.13\,h^{-1}\,{\rm Mpc}$ and $\gamma = 1.60 \pm 0.07$. The last two data points were not included for the power-law fit because they are likely underestimated owing to the limited box-size. Our values of r_0 and γ agree well with the observational estimates of Adelberger et al. (2003) and Adelberger et al. (2005), who measured the values of $r_0 = 4.0 \pm 0.6\,h^{-1}\,{\rm Mpc}$ and $\gamma = 1.57 \pm 0.14$ for the LBG ACF at $z \sim 3$, with a correction for the integral constraint.

The dark matter ACF (the red filled triangles in Figure 6) was also computed as described in Nagamine et al. (2008) in order to calculate the bias of LBGs against the dark matter distribution (see Section 8).

DLA auto-correlation

Similarly to the LBG ACF, it would be useful to compute the DLA ACF in order to estimate the DLA host halo mass. Observers also may be able to calculate the DLA ACF in the future when they accumulate a large enough sample of DLAs. In this

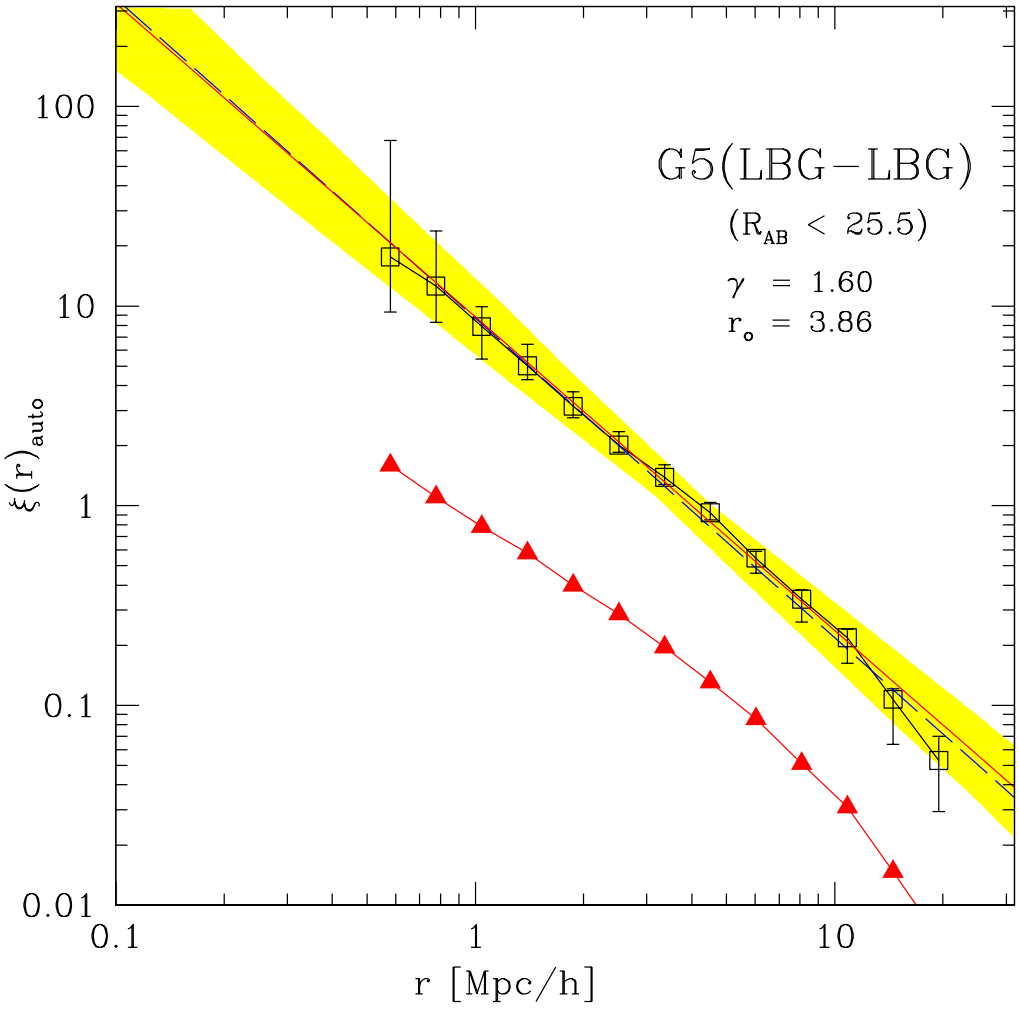

Figure 6 LBG auto-correlation function at $z = 3$ for the G5 run. The yellow shade shows the 1-σ range of the best-fitting power-law of Adelberger et al. (2005). The variance of the ACF using 100 random seeds is shown with vertical errorbars. The red solid and blue dashed lines are the best-fitting power-laws of Adelberger et al. (2005) and this work, respectively. The last two data points were not included for the power-law fit. The red filled triangles show the dark matter ACF at the same redshift.

section, we calculate the DLA ACF with both the unweighted and the $\sigma_{\rm DLA}$-weighted methods. By replacing all subscripts to 'DLA' in Equations (2) and (3), we obtain

$$\xi_{\rm DLA-DLA}(r) = \frac{D_{\rm DLA}D_{\rm DLA} - 2D_{\rm DLA}R_{\rm DLA} + R_{\rm DLA}R_{\rm DLA}}{R_{\rm DLA}R_{\rm DLA}} \tag{2}$$

and

$$\xi^{\rm weighted}_{\rm DLA-DLA}(r) = \frac{N_iN_jD^i_{\rm DLA}D^j_{\rm DLA} - 2N_iN_jD^i_{\rm DLA}R^j_{\rm DLA} + N_iN_jR^i_{\rm DLA}R^j_{\rm DLA}}{N_iN_jR^i_{\rm DLA}R^j_{\rm DLA}}, \tag{3}$$

where $N_iN_jD^i_{\rm DLA}D^j_{\rm DLA}$ and $N_iN_jD^i_{\rm DLA}R^j_{\rm DLA}$ are the numbers of data-data pairs and data-random pairs, weighted by the number of DLA pixels N_i and N_j. As before, 100 different realizations of random dataset have been used to examine the statistical variance.

Our DLA ACF result is shown in Figure 7, and we find the best-fitting power-law parameters (see Section 5 for confidence limit statistics) of $r_0 = 2.50 \pm 0.03\,h^{-1}\,$Mpc and $\gamma = 1.63 \pm 0.02$ for the unweighted ACF, and $r_0 = 2.87 \pm 0.05\,h^{-1}\,$Mpc and $\gamma = 1.63 \pm 0.03$ for the $\sigma_{\rm DLA}$-weighted ACF, as summarized in Table 5. The values of γ are similar to those for the LBG ACF with $\gamma \simeq 1.6$, but r_0 is much smaller. This is owing to the lower average DLA halo mass compared to the LBG host haloes, as we will discuss further in Section 8.

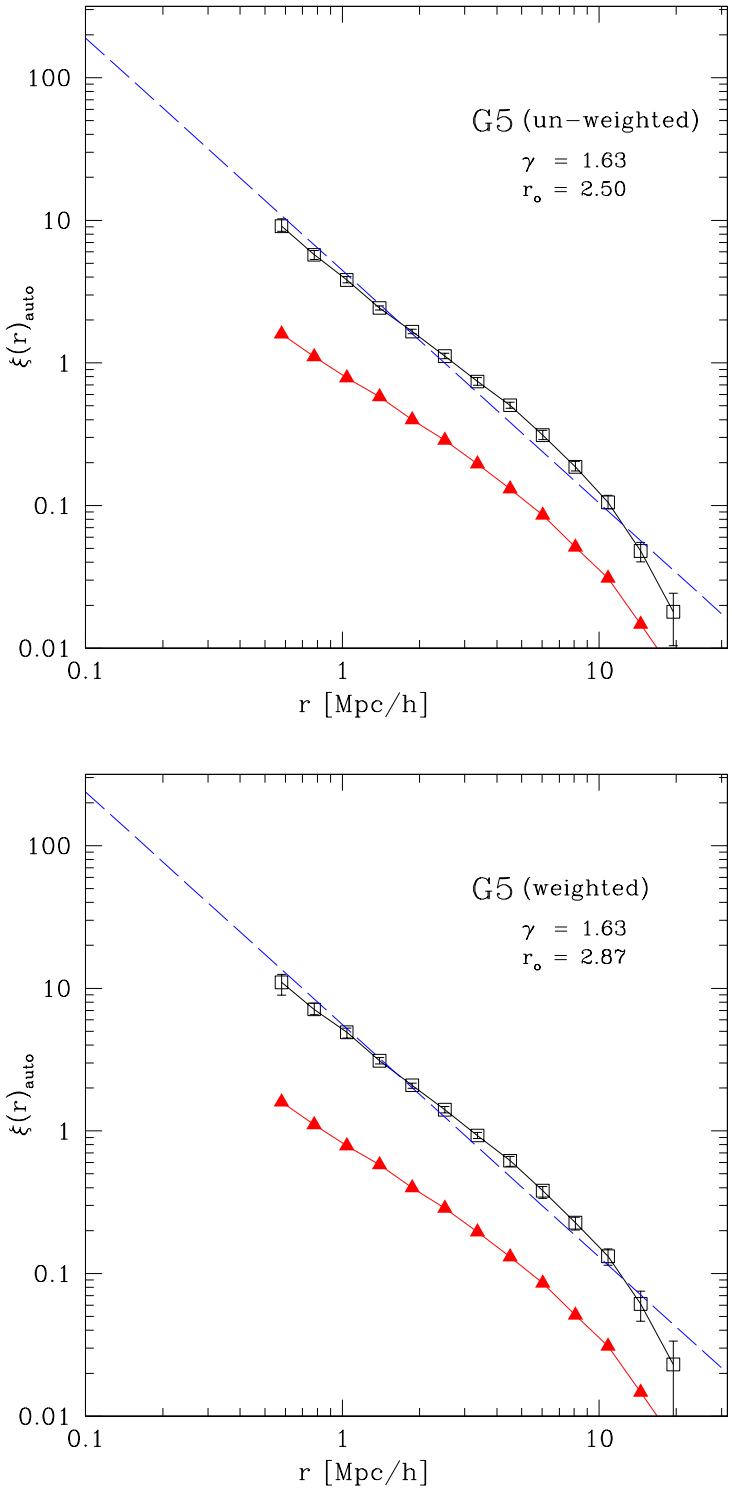

Figure 7 DLA auto-correlation function calculated with *unweighted* and $\sigma_{\rm DLA}$-*weighted* method for the G5 run. The variance of ACFs using 100 random seeds is shown with vertical errorbars. The blue dashed lines are best-fits for this work.

	r_0	γ
LBG-auto	3.86 ± 0.13	1.60 ± 0.07
DLA-auto (unweighted)	2.50 ± 0.03	1.63 ± 0.02
DLA-auto ($\sigma_{\rm DLA}$-weighted)	2.87 ± 0.05	1.63 ± 0.03

Table 5 ACFs of LBGs and DLAs for the G5 run. The results of unweighted and $\sigma_{\rm DLA}$-weighted methods are given for the DLA ACF. r_0 is in units of $h^{-1}\,$Mpc. The confidence limit statistics are described in Section 5. For comparison, Adelberger et al. (2005) reported $r_0 = 4.0 \pm 0.6\,h^{-1}\,$Mpc and $\gamma = 1.57 \pm 0.14$ for the LBGs at $z \simeq 3$.

CHAPTER 8

BIAS AND HALO MASSES

Comparing the correlation functions of DLAs and LBGs with that of dark matter gives the measure of 'bias' for the spatial distribution of these populations against that of dark matter. Figure 8 shows the bias, defined as $b \equiv \sqrt{\xi_i / \xi_{\rm DM}}$, as a function of distance r, where i = LBG or DLA. This definition is based on the linear bias model,

$$\xi_i(r) = b_i^2 \, \xi_{\rm DM}(r). \tag{1}$$

The corresponding expression for the cross-correlation is (Gawiser et al., 2001)

$$\xi_{\rm DLA-LBG}(r) = b_{\rm DLA} \, b_{\rm LBG} \, \xi_{\rm DM}(r). \tag{2}$$

Therefore, the two lines for the CCF in Figure 8 are in fact showing $\sqrt{b_{\rm DLA} b_{\rm LBG}}$, as indicated on the axis on the right-hand-side. Taking the ratio of the above two expressions gives (Cooke et al., 2006b)

$$\frac{\xi_{\rm DLA-LBG}(r)}{\xi_{\rm LBG}} = \frac{b_{\rm DLA}}{b_{\rm LBG}}. \tag{3}$$

In all cases shown in Figure 8, the bias slowly decreases with increasing distance. The upturn at $r = 20\,h^{-1}\,$Mpc for the LBG ACF is probably just noise. We take a simple average of bias values across the logarithmic bins at $r = 1.40 - 14.5\,h^{-1}\,$Mpc, and find $\bar{b} = 2.65$, 2.48, 2.24, 2.17 and 1.94 for LBG ACF, DLA-LBG CCF ($\sigma_{\rm DLA}$-weighted), DLA-LBG CCF (unweighted), DLA ACF ($\sigma_{\rm DLA}$-weighted), and DLA ACF (unweighted), respectively. The values of r_0 also reflect the sizes of average bias values. We took the above range of scales for taking the average because most of the recent observations are probing the scale of $r \simeq 1 - 10\,h^{-1}\,$Mpc.

Gawiser et al. (2007) used the results of Adelberger et al. (2005) to obtain an average bias of $\bar{b}_{\rm LBG} = 2.5 \pm 0.4$ for LBGs at $z \sim 3$. Our average bias value of 2.60

for the LBG ACF is very close to that of Adelberger et al. (2005), and at the lower end of the estimate of $\bar{b}_{\rm LBG} = 3.0 \pm 0.5$ by Lee et al. (2006)

The model of Sheth & Tormen (1999) shows that an understanding of the unconditional mass function can provide an accurate estimation of the large-scale bias factor. From our average bias, we calculate the mean halo mass for LBGs and DLAs (using the unweighted and the $\sigma_{\rm DLA}$-weighted results) based on the method described in Mo & White (2002), as shown in Table 6. Our calculation of LBG halo mass is very close to that by Adelberger et al. (2005), $M_{\rm halo}^{\rm LBG} = 10^{11.2} - 10^{11.8} M_\odot$ (yellow shade in Fig. 8), which is very encouraging. Finally, Bouche et al. (2005) estimated $\langle \log M_{\rm DLA} \rangle = 11.13 \pm 0.13$ from observations and $\langle \log M_{\rm DLA} \rangle = 11.16$ from simulations. These values are somewhat higher than the upper limit of our unweighted DLA halo mass and close to our $\sigma_{\rm DLA}$-weighted one. Cooke et al. (2006a) also obtained a similar value of $M_{\rm halo} \simeq 10^{11.2} M_\odot$.

Alternatively, we can directly calculate the mean DLA halo mass using the simulation result without going through the bias argument. For the G5 run, the mean is $\log\langle M_{\rm halo}^{\rm DLA} \rangle = 11.5$ and $\langle \log M_{\rm halo}^{\rm DLA} \rangle = 11.3$. These values are somewhat higher than the mean halo mass reported in Table 6. However, the values of $\langle M_{\rm halo} \rangle$ in Table 6 are computed from the average bias within the range of $r = 1.40 - 14.5\, h^{-1}\,$Mpc, and they could become higher if we included the bins at smaller scales. Since observers probe mostly $r \simeq 1 - 10\, h^{-1}\,$Mpc, the values reported in Table 6 are more appropriate for comparison with observations.

Bouche & Lowenthal (2004) defined the parameter α as the ratio of correlation functions: $\alpha \equiv \overline{b}_{\rm CCF}(M_{\rm DLA})/\overline{b}_{\rm ACF}(M_{\rm LBG})$. If the value of α is larger (or smaller) than unity, then the mean halo mass of DLAs is more (or less) massive than that of the LBGs. The ratio of the average bias of LBG ACF and DLA-LBG CCF is $\alpha = 0.727$ for our results. This value is in good agreement with the observational estimates of

	$\overline{bias}$	$\log\langle M_{\rm halo}\rangle$
LBG-auto	$2.67^{+0.28}_{-0.06}$	$11.53^{+0.22}_{-0.06}$
DLA-auto (unweighted)	$1.94^{+0.11}_{-0.13}$	$10.71^{+0.16}_{-0.19}$
DLA-auto ($\sigma_{\rm DLA}$-weighted)	$2.17^{+0.14}_{-0.13}$	$11.02^{+0.14}_{-0.16}$

Table 6 Average biases and halo masses of LBGs and DLAs for the G5 run. The plus and minus values next to the average bias show the upper and lower limits at $1.40 < r < 14.5\ h^{-1}\,$Mpc. Mean halo masses are computed from the second column following Mo & White (2002) and given in units of $M_\odot$.

$\alpha = 1.62 \pm 1.32$ (Bouche & Lowenthal, 2004), $\alpha = 0.73 \pm 0.08$ (Bouche et al., 2005), and $\alpha = 0.771$ (Bouche et al., 2005; Mo & White, 2002).

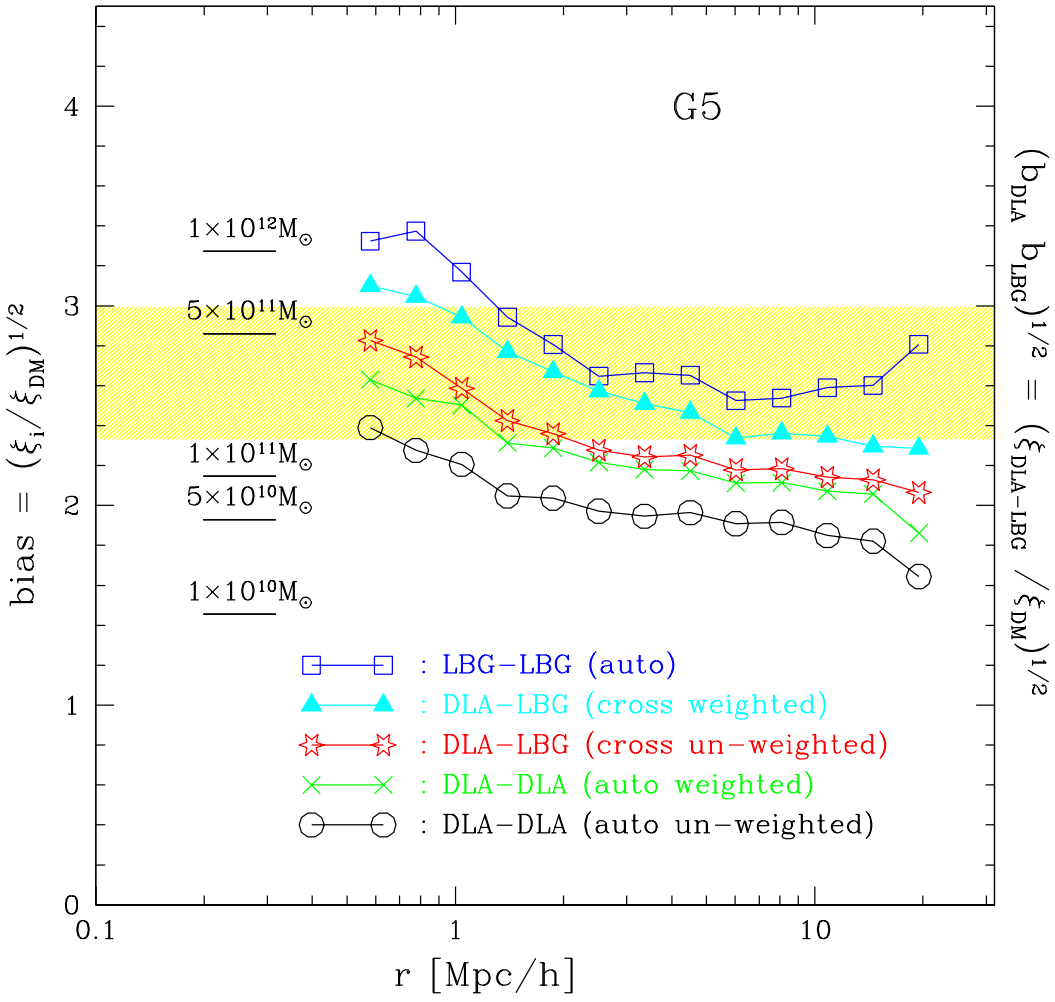

Figure 8 The biases of all correlation functions at $z = 3$ that we computed in this paper for the G5 run. The tick marks on the left-hand-side show the host halo masses calculated with the method described in Mo & White (2002). The yellow shade shows the upper and lower limits by Adelberger et al. (2005).

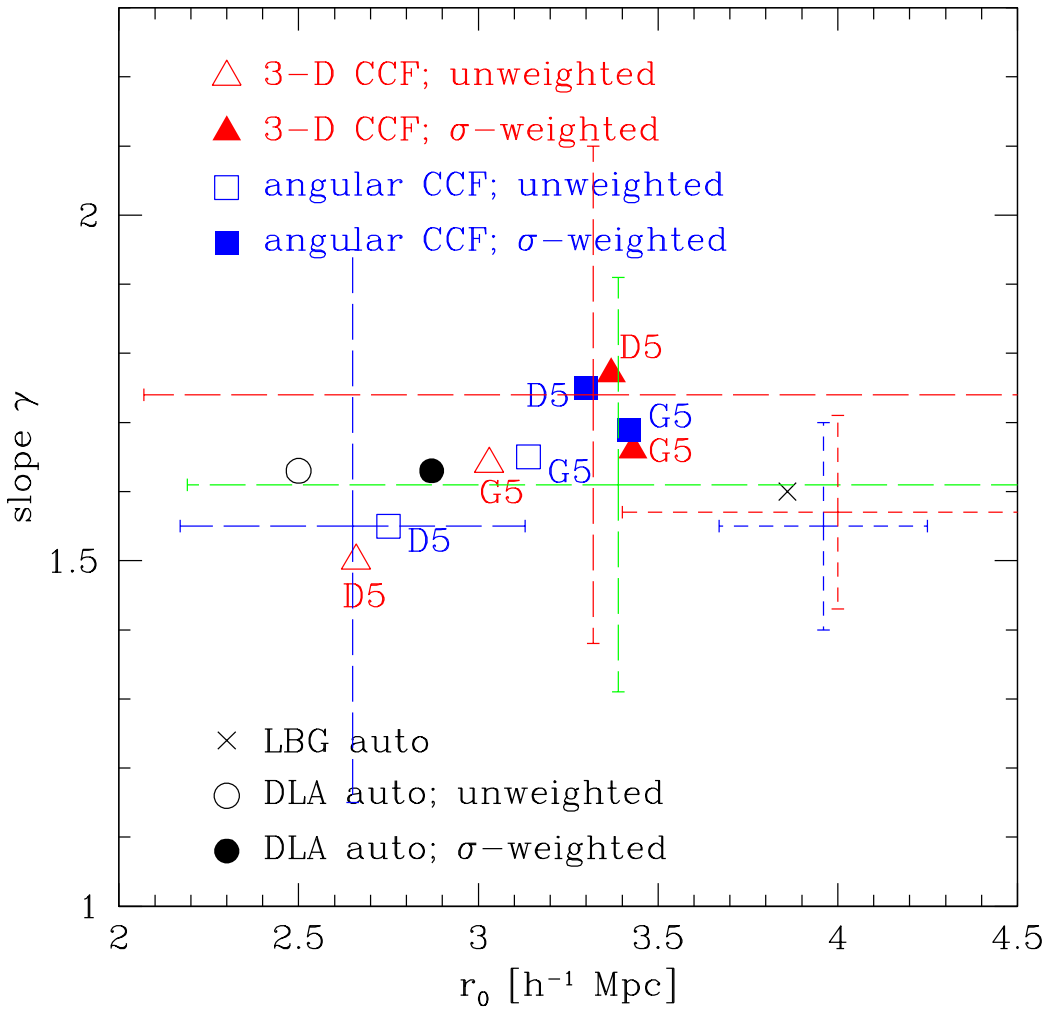

Figure 9 Summary of best-fitting power-law parameters for all correlation functions that we obtained in earlier sections. Long blue, red, and green dashed cross lines are for the LBG ACF, the angular CCF, and the 3-D CCF of Cooke et al. (2006a,b), respectively. The LBG ACF of Adelberger et al. (2003) is shown in a short blue dashed line and of Adelberger et al. (2005) is shown in red.

CHAPTER 9

PART I: SUMMARY AND CONCLUSION

Our study represents a first attempt to calculate the DLA-LBG cross-correlation function at $z = 3$ using cosmological SPH simulations. We calculated the DLA-LBG CCFs in several different approaches: 3-D, angular, unweighted, and $\sigma_{\rm DLA}$-weighted. We also computed the auto-CF of LBGs and DLAs, and the bias against dark matter. In comparison to the observational data by Adelberger et al. (2005); Cooke et al. (2006a,b), we find good agreement between our simulations and observational measurements. Our results suggest that the spatial distribution of DLAs and LBGs are strongly correlated.

Let us summarize some of the main conclusions of this work. In the first part of this paper, our results on the 3-D CCF calculated with spherical shells (Table 3) are to be compared with the 3-D spherical shell result by Cooke (private communication), $r_0 = 3.39 \pm 1.2\,h^{-1}\,{\rm Mpc}$ and $\gamma = 1.61 \pm 0.3$. Our results are consistent with Cooke's within the error. The shallow slope of Cooke's above estimate probably owes to the limited sample size in the spherical shell at small distances, as we discussed in Sections 4 and 6.

In the second part, we have replaced the spherical shell method with the projected approach used in Adelberger et al. (2003) and Cooke et al. (2006b), and calculate the best-fitting values given in Table 4. Encouragingly, our results are within the upper and lower limits of the observational measurement by Cooke et al. (2006a,b). We corrected all CFs in this paper with the integral constraint.

Finally, we also analyzed the auto-correlation functions of LBGs and DLAs at $z = 3$ (Table 5) found in our simulations. Our results for the best-fitting parameters of the LBG ACF agree well with Adelberger et al. (2005). Our results show that LBGs are more strongly correlated than DLAs, and have higher mean halo mass.

Figure 9 summarizes the best-fitting power-law parameters for all the correlation functions that we obtained in the earlier sections. In most cases, the slope γ falls into the range $\approx 1.5 - 1.7$ and the variation is not very large. The correlation length r_0 shows a larger variation from $2.5\,h^{-1}$ Mpc to $4\,h^{-1}$ Mpc, depending on the sample and calculation method. This trend is similar to that seen by Cooke et al. (2006b, Fig. 8). In general, the $\sigma_{\rm DLA}$-weighted method gives a larger r_0 than the unweighted method.

Finally, the LBG bias, derived from the LBG ACF in Section 8, has led to the upper and lower limits of the LBG dark matter halo mass of $\log\langle M_{\rm halo}\rangle = 11.53^{+0.22}_{-0.06}$ (see Table 6). This result is consistent with observational estimates of the LBG halo mass of $M_{\rm halo} \sim 10^{12} M_{\odot}$, (e.g., Steidel et al., 1998; Adelberger et al., 1998) and within the limit of $M_{\rm halo} = 10^{11.2} - 10^{11.8} M_{\odot}$ (Adelberger et al., 2005). Similarly, we derived the DLA biases, and obtained the mean DLA halo masses as shown in Table 6. Cooke et al. (2006a)'s measurement showed a DLA galaxy bias of $b_{\rm DLA} \sim 2.4$ and an average DLA halo mass of $M_{\rm halo} \sim 10^{11.2} M_{\odot}$. Our average DLA bias ($\overline{b} = 1.94$ and $\overline{b} = 2.17$ for un-weighted DLA ACF and weighted DLA ACF, respectively) and halo mass estimates ($\log\langle M_{\rm halo}^{\rm DLA}\rangle$=10.71 and 11.02 for un-weighted DLA ACF and weighted DLA ACF, respectively) are in good agreement with theirs. We also examined the ratio of bias values defined as $\alpha \equiv \overline{b}_{\rm CCF}/\overline{b}_{\rm ACF}$ (Bouche & Lowenthal, 2004), and found that our value of $\alpha = 0.727$ agrees well with the observational estimates. This again shows that the mean halo mass of DLAs is less than that of the LBGs. The fact that $\langle M_{\rm halo}^{\rm LBG}\rangle$ is greater than $\langle M_{\rm halo}^{\rm DLA}\rangle$ is a natural outcome because the LBG sample is limited to the bright star-forming galaxies with $R_{\rm AB} < 25$ and $M_{\star} \simeq 10^{10} - 10^{11} M_{\odot}$, whereas the DLA H I gas is present in numerous lower mass halos below the LBG threshold.

Our simulations are able to reproduce the physical properties of LBGs such as

stellar mass, SFR, and colours (Nagamine et al., 2004). In this work, we followed another observational method, i.e. DLA-LBG CCF, to examine the consistency between observations and simulations. We found good agreement between our results and observations. Furthermore, there are accumulated evidences that suggest a high halo mass for LBGs (e.g., Mo & Fukugita, 1996; Adelberger et al., 1998; Baugh et al., 1998; Giavalisco et al., 1998; Steidel et al., 1998; Kauffmann et al., 1999; Mo et al., 1999; Katz et al., 1999; Papovich et al., 2001; Shapley et al., 2001). Therefore, the scenario that the majority of LBGs is merger-induced starburst systems associated with low-mass haloes (Lowenthal et al., 1997; Sawicki & Yee, 1998; Somerville et al., 2001; Weatherley & Warren, 2003) no longer appears to be a viable model for LBGs.

In our simulations, we estimated the H I column densities using a pixel size that is much larger than the typical quasar beam size, which is of the order of parsecs. This may have some impact on our estimates of $N_{\rm HI}$ and the corresponding statistics such as the H I column density distribution function. For example, if the ISM is clumpy on smaller scales than our pixel size, there could be high-density neutral clouds below our resolution scale that are self-shielded and contain larger amounts of H I . Unfortunately, owing to limitations in computational resources, it is not possible for us at the moment to run such a high-resolution cosmological simulation with the same box size as we have used in this paper. In future work, we will nevertheless attempt to check the dependence of our $N_{\rm HI}$ estimates on numerical resolution, and perform more rigorous resolution tests.

CHAPTER 10

PART II: INTRODUCTION

Over two decades earlier than *Spitzer Space Telescope* (hereafter *Spitzer*), the *Infrared Astronomical Satellite* (*IRAS*) observed the local universe ($0 < z < 0.2$) (Hacking et al., 1987; Saunders et al., 1990) at far-infrared (60 μm), and Fang et al. (1998) and Shupe et al. (1998) constructed models to estimate the mid-infrared (12 μm and 25 μm) contribution to the total energy spectrum using a sample of 668 galaxies from the IRAS Faint Source Survey. The *Infrared Space Observatory* (*ISO*) allowed the first deep surveys of galaxies in the mid-infrared (MIR) and far-infrared (FIR) up to $z \sim 1$ (Elbaz et al., 1999; Puget et al., 1999). The deepest survey of 15 μm probed the evolution of Luminous Infrared Galaxies (LIRGs) and Ultra Luminous Infrared Galaxies (ULIRGs), showing that the dust-enveloped starburst galaxies are undergoing intense evolution in luminosity and in density (Elbaz et al., 2002).

The significant improvement in sensitivity and resolution (from 3.6 μm to 160 μm) of *Spitzer* over its predecessors has significantly extended the earlier IR astronomy. The *Spitzer* observations by took in recent years at near-infrared (NIR), MIR, and FIR wavelengths revealed that dust is an important component of the interstellar medium (ISM) and the inter galactic medium (IGM) in the formation and evolution of galaxies. The *Spitzer* surveys have enabled to observe the evolution of galaxy luminosity function (LF). Using the 24 μm source catalogues with redshift information, Le Floc'h et al. (2005) presented the evolution of IR LFs out to $z \sim 1$ for 15 μm and total IR. In the redshift range between 0 and 3, based on the IR photometric redshift, Pérez-González et al. (2005) obtained the LF at rest frame 12 μm. The LFs rest frame 8 μm of star forming galaxies at $z \sim 1$ and $z \sim 2$ have been presented by Caputi et al. (2007). Babbedge et al. (2006) computed the MIR galaxy LF out to

$z \sim 1$ based on the SWIRE EN1 field dataset and using photometric redshifts.

Considering the dust extinction effect, a large portion of the energy emitted by dust in galaxies has been discovered. The energy density under FIR is comparable to that in the optical and NIR Hauser et al. (1998). This finding revealed the importance of the IR radiation as much as the ultra-violet (UV) and the optical radiation from galaxies. In particular a large fraction of UV emission from young stars is absorbed by dust and re-emitted as an IR radiation, and the resulting shape of spectral energy distribution (SED) is often times significantly altered from the original SED. Therefore, it is crucial to correct for the IR dust emission when estimating the star-formation rates and star-formation histories. The presence of dust promotes star formation by shielding dense clouds from stellar UV radiation and keeping the clouds of low temperatures.

Infrared emission reprocessed by dust is over a half of the total stellar energy output in the Universe. The earlier work by Nagamine et al. (2004, 2005a,b) showed a reasonable agreement between cosmological simulations and observations regarding the space density of star-forming galaxies, but the differential distribution of sources among different types (e.g. LBG vs. submm galaxies) was still unclear. Clarifying the contribution of IR-bright galaxies to the total SFR is an important topic in galaxy formation.

The part II of this dissertation is organized as follows. In Chapter 11, we describe the features of the GRASIL code (Silva et al., 1998). In Chapter 12, we report comparing results of computed galaxy LFs with the *Spitzer* observations. Finally, we present and discuss our conclusion in Chapter 13.

CHAPTER 11

SIMULATION

For the second part we utilize three different SPH simulations and use the computed physical properties (e.g. stellar mass, formation time, and metallicity) of the galaxy population at different redshifts carried out under GADGET-3 (Springel, 2005) and combine it with the spectrophotometric code GRASIL (Silva et al., 1998) to compute the detailed SEDs of model galaxies. The simulation parameters of the three runs (N144L10w5psfmcvw1.5ME, N216L10w5psfmcvw1.5ME, and N400L100w5psfmcvw1.5ME) are summarized in Table 7 and Table 8 (Choi & Nagamine, 2009a,b, 2010). In the next two section we give an overview of GRASIL and the interfacing technique between GADGET and GRASIL.

GRASIL

We compute the spectral energy distribution using the spectrophotometric GRASIL code (Silva et al., 1998), which follows the evolution of the stellar population and SED taking into account the extinction and emission by dust. During certain phases of

Run	$L_{\rm box}$	$N_{\rm p}$	$m_{\rm DM}$	$m_{\rm gas}$	ϵ
N144L10	10.00	2×144^3	2.42×10^7	3.72×10^6	2.78
N216L10	10.00	2×216^3	5.96×10^6	1.21×10^6	1.85
N400L100	100.00	2×400^3	9.12×10^8	1.91×10^8	6.45

Table 7 Simulations employed in the part II. $N_{\rm P}$ is the initial number of gas and dark matter particles (hence $\times 2$). $m_{\rm DM}$ and $m_{\rm gas}$ are the masses of dark matter and gas particles in units of $h^{-1}M_{\odot}$, respectively. ϵ is the comoving gravitational softening length in units of $h^{-1}kpc$, which is a measure of spatial resolution. All runs adopt a strong galactic wind feedback model.

	High density		Low density	
Model	η	ζ	η	ζ
1.5ME	Momentum	1.5	Energy	1

Table 8 The wind model adopted for the part II. The parameter η is the mass-loading factor, and ζ is the scaling parameter for the wind velocity (Choi & Nagamine, 2009a).

galaxy evolution, AGN activity might contribute to shape the observed SEDs of the galaxy and to provide an additional point-like source in the center of the galaxy and to supply additional heating source of galactic dust, but presently, we do not consider this complication, which we postpone to future investigation.

To estimate the SED of a galaxy at certain epoch t_g, first, the history of the star formation rate (SFR) $\phi(t)$, the initial mass function (IMF), the metallicity $Z(t)$, and the residual gas fraction must be determined. Second, the integrated SED of the galaxy must be estimated by coadding the SEDs of all the stars.

The chemical evolution is a main step for spectrophotometric model. The code describes one-zone (no dependence on space, only on time) open models with the infall of primordial gas. According to the standard equations of galactic chemical evolution, the total gas mass $m_g(t)$ and of the amount of certain gas element $x_i(t)$ in terms of quantities at time t (i.e. as a function of the previous history of the galaxy):

$$\dot{m_{g,i}} = \dot{m}_{g,i}|_{SF} + \dot{m}_{g,i}|_{FB} + \dot{m}_{g,i}|_{Inf} \tag{1}$$

where $\dot{m}_{g,i}|_{SF}$ is the consumption of gas caused by the formation of new star, $\dot{m}_{g,i}|_{FB}$ is the feedback to the ISM due to the final stages of stars, and $\dot{m}_{g,i}|_{inf}$ is the infalling primordial gas to form the galaxy.

GRASIL assumes a Schmidt-type SFR that consists of two terms $\phi(t) = \nu m_g(t)^k + f(t)$. The first term is a Schmidt law, and the second term is an analytical function, which is expressed as a constant or exponential function of time. The second term

can be applied to introduce a burst of star formation over a quiet evolution. The infall gas mass into galaxies is expressed as $\dot{m}_{g,i}|_{inf} = x_{i,inf} m_{inf} exp(-t/\tau_{inf})$ where $x_{i,inf}$ is the mass fraction of element i, m_{inf} is the infall mass at time t_{inf}, and τ_{inf} is the exponential infall timescale.

The single stellar populations (SSPs) incorporated in GRASIL are based on the Padova stellar models (Bertelli et al., 1994) and deal with a large range in ages t, from 1 Myr to 18 Gyr and in metallicity, $Z(t) = 0.0001$, 0.0004, 0.0008, 0.004, 0.008, 0.02, 0.05, to reproduce age and composition of the stellar content of galaxy (the relative proportion of the metals equal to the solar matallicity). The SSPs cover the asymptotic giant branch (AGB) isochrones that include handling of the dusty envelope around AGB stars and have been corrected under the recent data of star clusters in the large magellanic cloud (Marigo et al., 2008). Normally, the spectral synthesis method consists in summing up the spectra of each stellar population provided by a SSP of age and metallicity, weighted by the SFR at time of the star birth (e.g., Bressan et al., 1994):

$$F_\lambda(t_g) = \int_0^{t_g} SSP_\lambda[t_g - t, Z(t)]\phi(t)\mathrm{d}t, \tag{2}$$

where t_g is the age of the galaxy and t is the birth age of an individual SSP. But to keep dust into account, GRASIL must be specified with a dust model and geometry and solves the transfer equation for the radiation in presence of dust in the different phases for the ISM.

GRASIL calculates the radiative transfer of the starlight, the heating of the gains and the emission from these grains with a self-consistent calculation of grain temperature for an assumed geometrical distribution of the stars and dust (a specific grain model). The galaxy can be modeled in two main parts. To describe all different types of galaxies, Silva et al. (1998) have introduced a general geometry consisting in a disk and bulge system. The configuration of geometry and galaxy components is

illustrated in Figure 10.

The disk is described by radially and vertically exponential profiles,

$$\rho = \rho_o exp(-R/R_{sl}) exp(-|z|/z_{sl}), \tag{3}$$

where the radial scale-length R_{sl} and vertical z_{sl} are free parameters and can be independently set for the three components. In the case of bulge (or elliptical) GRASIL adopts spherical symmetric distributions with King Profile:

$$\rho_b = \rho_0 (r^2 + r_c^2)^{-3/2}, \tag{4}$$

where the scale-length r_c is a core radius and free parameter.

The cold gas and dust in a galaxy are assumed to be in a two-phase medium. The medium consists of dense gas in giant molecular clouds embedded in a lower density diffuse component. Stars are assumed to be formed inside molecular clouds (MCs) and continuously escape into the diffuse medium on a time-scale t_{esc}. Dust is assumed to be a mixture of carbonaceous and silicate grains and polycyclic aromatic hydrocarbon (PAH) molecules. The carbonaceous grains are considered to have the optical properties of randomly oriented graphite, and the silicate grains are considered to have no clearly defined shape (their sizes vary between $8\mathring{A}$ and $0.25\mu m$). The fixed grain size distribution is selected to match the mean dust extinction curve and emission in the local ISM. Then, the SED of the dust emission is computed over different types of grains from UV to the submm. GRASIL has been demonstrated to provide an excellent match to the observationally measured SEDs (Bressan et al., 2002).

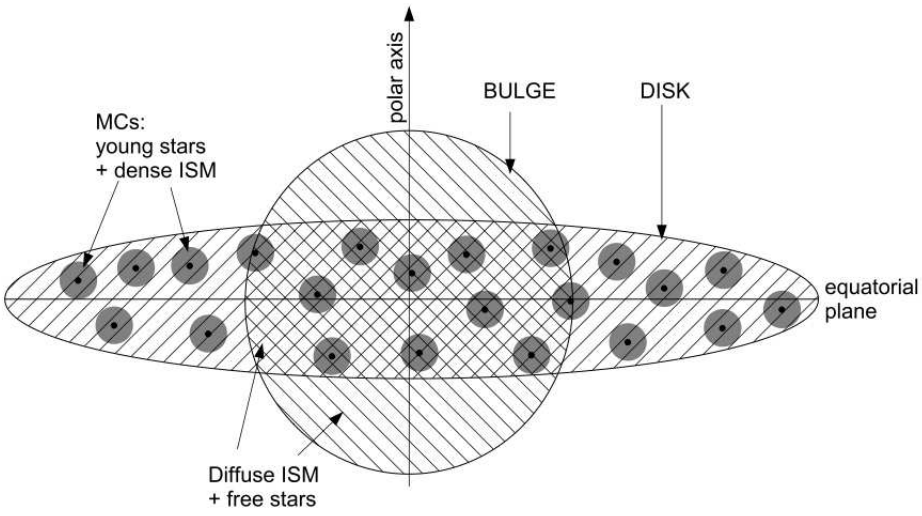

Figure 10 Illustration of the adopted geometrical distribution (Silva et al., 1998)

Interfacing between GADGET and GRASIL

To compute the statistical properties of the galaxy distribution from hybridizing GADGET and GRASIL codes, we first run GADGET and generate a set of data called snapshot at certain redshift and then run GRASIL. The simulation will produce a set of timeline snapshots with different box sizes and particle numbers. It will create a star particle when a set of criteria (such as fast cooling and Jeans instability) is satisfied in dense and cold gas clouds. Each star particle has properties of stellar mass, formation time, and metallicity. A collection of star particles will be treated as a galaxy, which can be indentified by a grouping algorithm. We compute SEDs of different time epochs and obtain a good coverage of all the different metallicitis with certain geometry of star particles under assumption of a Salpeter Initial Mass Fuction (IMF). The main parameters we have used for this work are summarized in Table 11. This set of SEDs acts as a look-up table that consists of the time evolutions and metallicities. The outputs from GADGET compare with the SED look-up table,

and we sum up each SED of star particles to create the final one. Once we calculate the SEDs for the star particle group. We compute the luminosity and AB magnitude in different observed IR bands (IRAC and MIPS) by combine the SED with the filter/detector response function (Figure 11).

Parameters	Valuses	Definitions
t_{fin}	13.0	final galactic age (Gyr)
i_{sfrm}	1.0	0 → nothing, 1 → simple Schmidt
i_{sfrt}	0.0	0 → nothing, 1 → constant, 2 → exponential
k_{sch}	1.0	exponent of schmidt law
τ_{inf}	0.001	exponential infall timescale (Gyr)
m_{inf}	1.0E11	infall mass ($M_{\odot}$)
tgal	13.0	Age of the model in Gyr
igeo	1	geometry setting

Table 9 Parameters for the GRASIL code

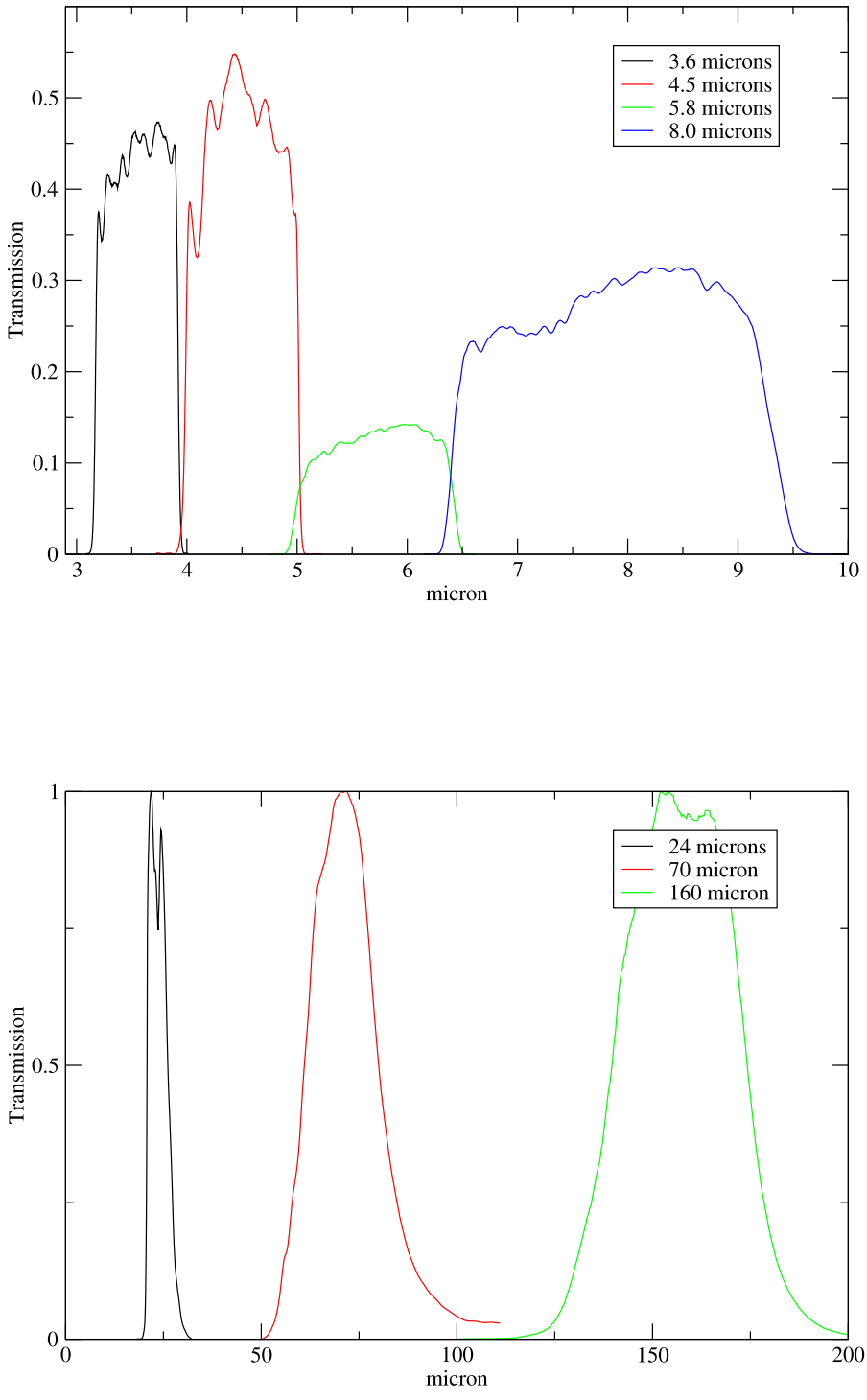

Figure 11 Filter functions of IRAC and MIPS of *Spitzer*.

CHAPTER 12

SPECTRAL ENERGY DISTRIBUTIONS

By modifying the GRASIL code, we are sequentially able to generate the time evolution of spectral energy distributions (SEDs) of the specified metallicity and geometry. Figure 12 shows SEDs of the metallicity Z=0.0001 and time epochs from 1 to 12 Gyrs with 1 Gyr interval. The upper left panel shows the SEDs of starlight extincted, and the molecular clouds (MCs) and cirrus (diffuse gas) emissions are shown in the upper right and lower left panels, respectively. The total of all three emissions are illustrated on the lower right.

Luminosity Functions

Galaxies of all types come in a rage of luminosities, masses, and sizes. Among these variables, the total luminosity of a galaxy is most directly measurable one and supplies physical guideline at certain redshift z. In the following two sections, we show a conversion method between an AB magnitude and the luminosity L_λ and apply to snapshot data from GADGET. In the last section, we compare our computed results with real estimates from *Spitzer* data.

Calculation of the AB magnitude

We start our investigation with galaxy luminosity function (LF). First, we use two 10 Mpc h^{-1} box simulations at $z = 3$. The simulations contain 144^3 (N144) and 216^3 (N216) initial particle numbers of gas and dark matter particles. After we calculate total SED of each star particle cluster, the magnitude of star particles must be identified. To achieve the apparent magnitude, one needs to consider an object with SED $L_\lambda(\lambda, t)$ at redshift z. The apparent magnitude of the galaxy correlated to the collected photon at a certain redshift can be written as

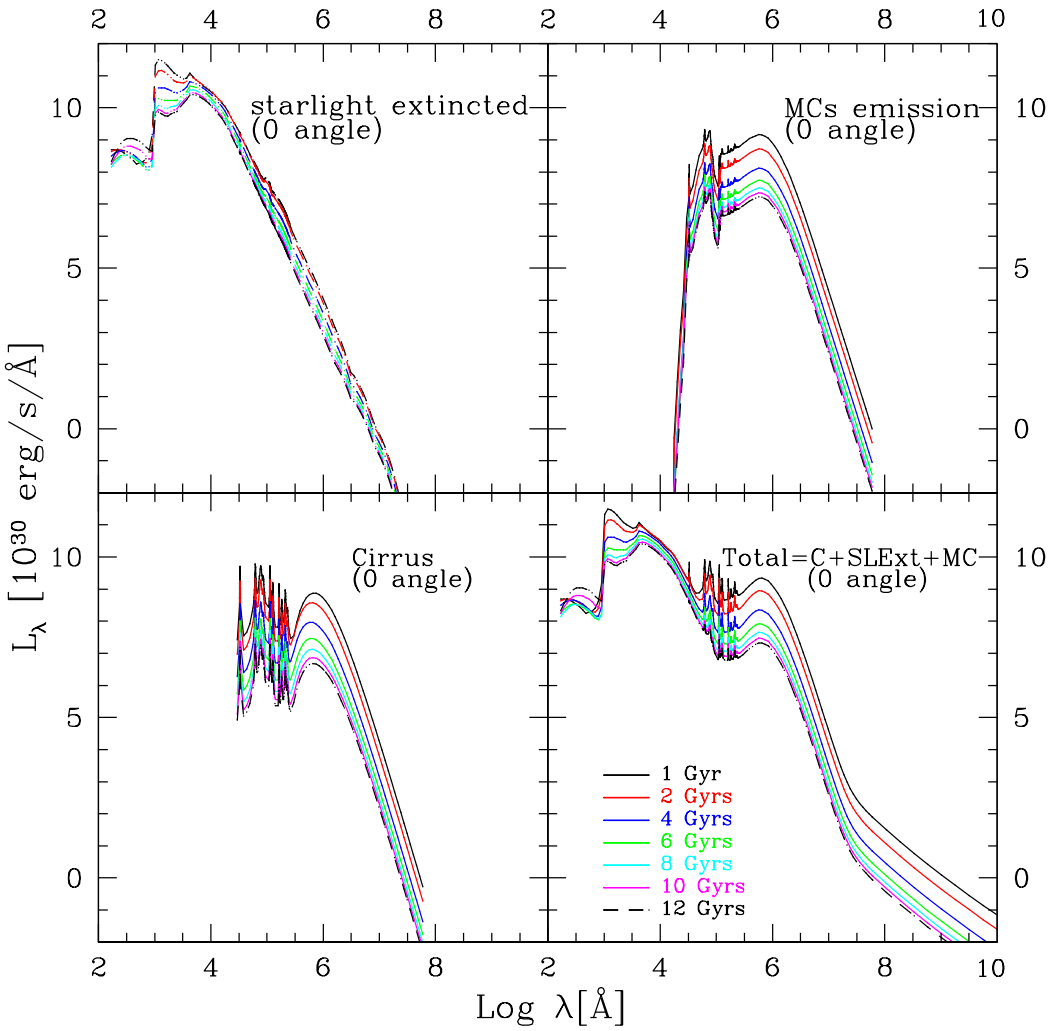

Figure 12 The time evolution of Spectral Energy distributions (SEDs) with starlight extinction, molecular cloud (MC) emission, and cirrus (diffuse gas) emission.

$$m(z,t) = -2.5log\frac{\int \frac{\mathrm{d}\nu}{\nu}\frac{(1+z)L_\nu[\nu(1+z),t]}{4\pi d_L^2}R(\nu)}{\int \frac{\mathrm{d}\nu}{\nu}C_\nu R(\nu)}, \quad (1)$$

where d_L^2 is the luminosity distance, R(ν) is a filter function, and $C_(\nu)$ is a fixed reference spectrum. For AB magnitude, the above equation is change to (Fukugita et al., 1996)

$$m_{AB}(z,t) = -2.5log\frac{\int \frac{\mathrm{d}\nu}{\nu}\frac{(1+z)L_\nu[\nu(1+z),t]}{4\pi d_L^2}R(\nu)}{\int \frac{\mathrm{d}\nu}{\nu}R(\nu)} - 48.6 \quad (2)$$

with C_ν correlated to the theoretical reference with constant flux density of $3.631 \times 10^{-20} erg^{-1}cm^{-2}$ Hz^{-1} (Oke & Gunn, 1983). Since SEDs from the GRASIL code are based on the wavelength λ, we need to change the second equation in terms of the luminosity L_λ. The converted AB magnitude is the following

$$m_{AB}(z,t) = -2.5log\frac{\int \frac{\mathrm{d}\lambda}{(1+z)}\frac{(\lambda L_\nu[\lambda(1+z)^{-1},t]}{4\pi d_L^2}R(\lambda)}{\int \frac{\mathrm{d}\lambda}{\lambda}R(\lambda)} - 22.407. \quad (3)$$

Application

Simulated Galaxy Luminisity Functions

Galaxy LFs in the four IRAC (3.6, 4.5, 5.8, and 8.0 μm) and three MIPS (24, 70, and 160 μm) bands are illustrated in Figure 13. Comparing two simulations, we see that the effects of the particle amounts on the apparent magnitude are noticeable. N144 particle simulation shows slightly brighter than N216 simulation while N216 has higher luminosity. From two figures, we observe that the longer wavelengths (MIPS bands) are significantly boosted. This comes from the bottom integral of AB magnitude calculated from L_λ, a shape of the SED (Figure 14), and the redshift z.

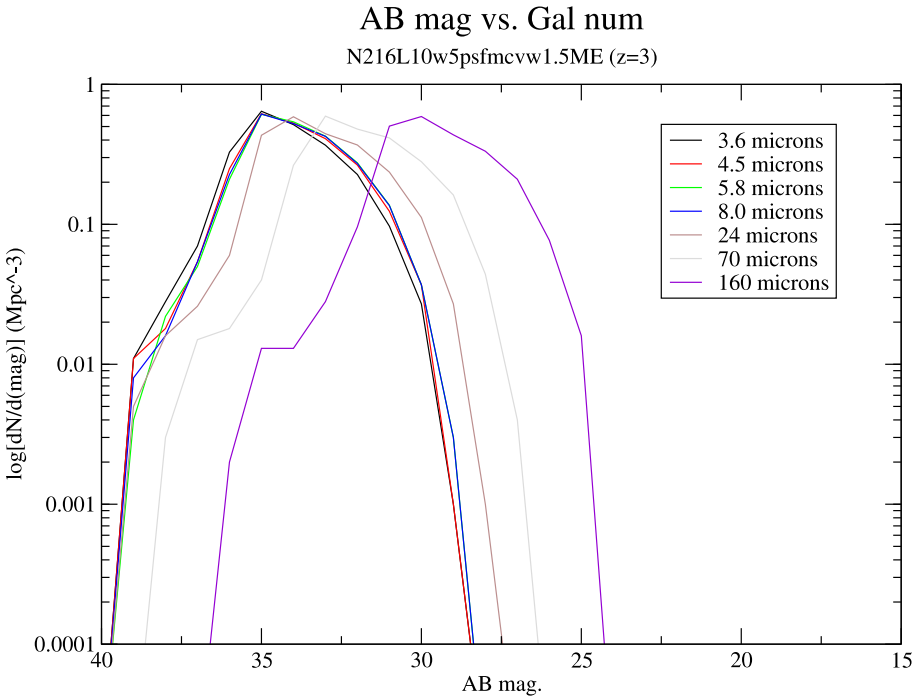

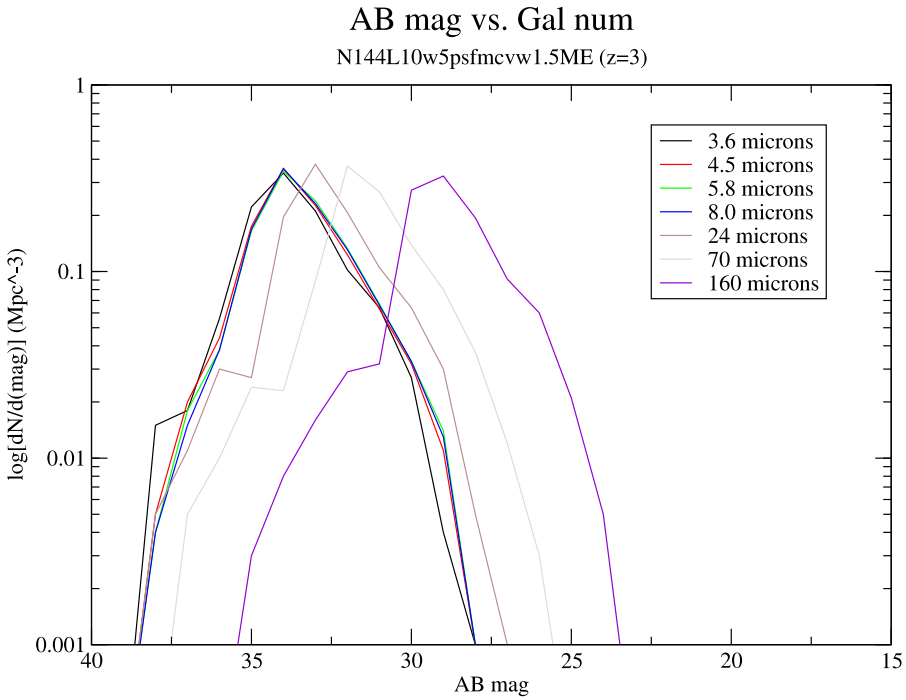

Figure 13 Galaxy number count in the four IRAC and three MIPS bands with particle numbers of 144^3.

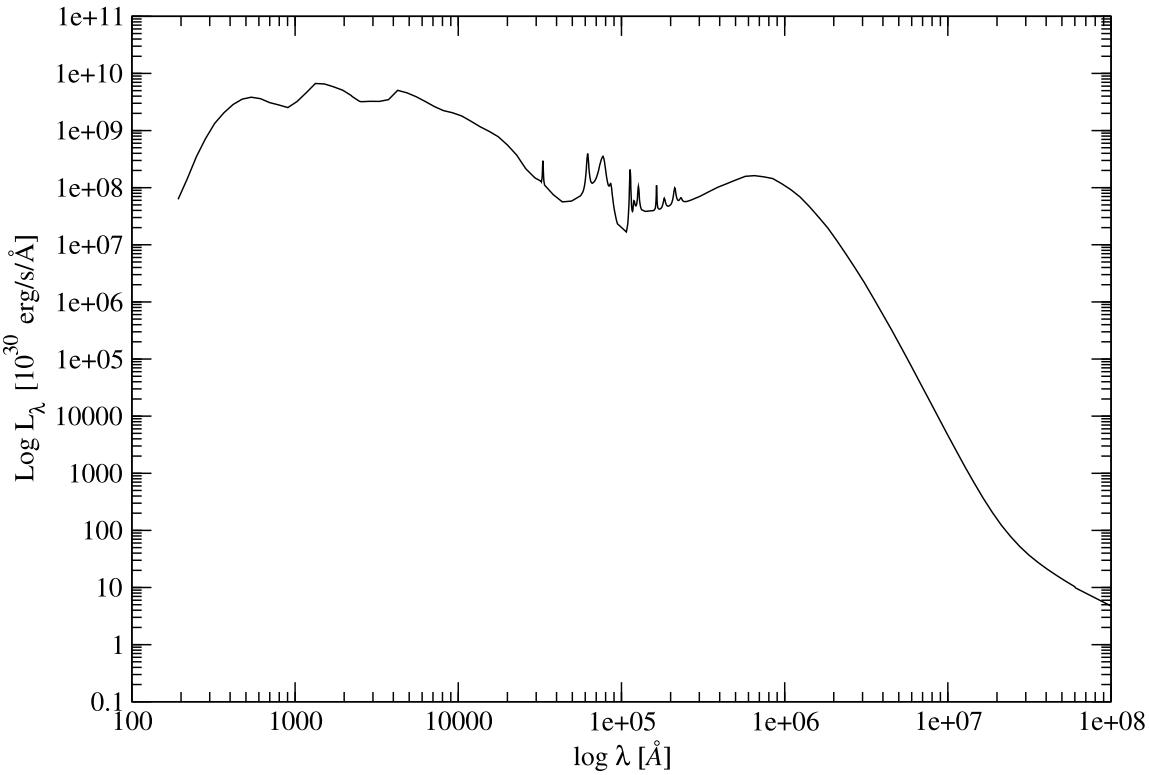

Figure 14 SED created by the GRASIL code at z=3 with 144^3 particle numbers and metallicity of Z=0.0001.

Mass, Metallicity, and Average formation time

The mass ($M_{\rm SP}$), metallicity (Z), and average formation time (t_{avg}) have been plotted against the AB magnitude. In Figure 15 the star particles (SPs) are distributed in a large mass range. The AB magnitude of N144 simulation SPs is higher than N216 ones. This is consistent with a galaxy number count result. It shows larger deviation at the lower mass. N216 simulation can resolve the low mass SP cluster even though cannot create the missive SPs. In Figure 16 we notice that there are two clearly separated groups of SPs in the N215 simulation. The majority of

active galaxies has the higher metallicity. The N144 simulation also shares the same trend as N216, but unlike N216 none of bright SP cluster in N144 reaches at the solar metallicity ($Z_{\odot}$=0.02) even with higher magnitude. Two graphs in Figure 17 provide a solution to the above question. From first panel of Figure 17, none of N144 SPs has the t_{avg} older than 1 Gyr. Since N144 run has small particle numbers, the collapsing time-scale is higher than N216, so it takes longer to form the SP clusters. Therefore, N144 is populated with younger SPs than N216 simulation and doesn't have enough time to create high metallicity.

The galaxy luminosity function at different time epoch

With the larger box size (100 Mpc h^{-1}) and more particle numbers (N400), we examine the evolution of the LFs in wavelength range of 8 μm and 24 μm. Our results in Figure 18 to Figure 19 are compared with available data in the published papers. At 8 μm (first panel of Figure 18) the rest-frame LF results at $z \sim 2.0$ from the combined dataset in GOODS-N and GOOD-S (Caputi et al., 2007) and from GOODS+VVDS-SWIRE (Rodighiero et al., 2009) are compared. We are in very good agreement with Caputi et al. 2007. Within the limits, we have a reasonable agreement with Rodighiero et al. 2009, still with some differences especially at the higher and lower ends of L_{λ} values. The comparison with Caputi et al. support our SPH simulations and the parameters used for the GRASIL code. At 24 μm (second panel of Figure 19) Rodighiero et al. (2009) sample provides nearly consistent results at the center part of their data with ours. The lower end is still a bit deviated from our result but not as much as the case of 8 μm, and the higher end is lower than

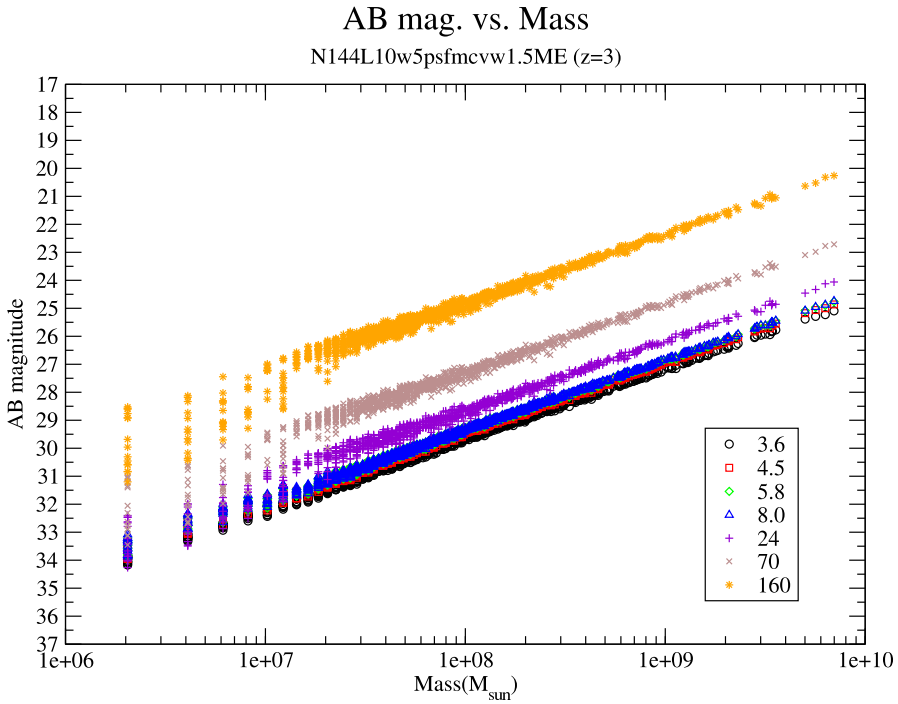

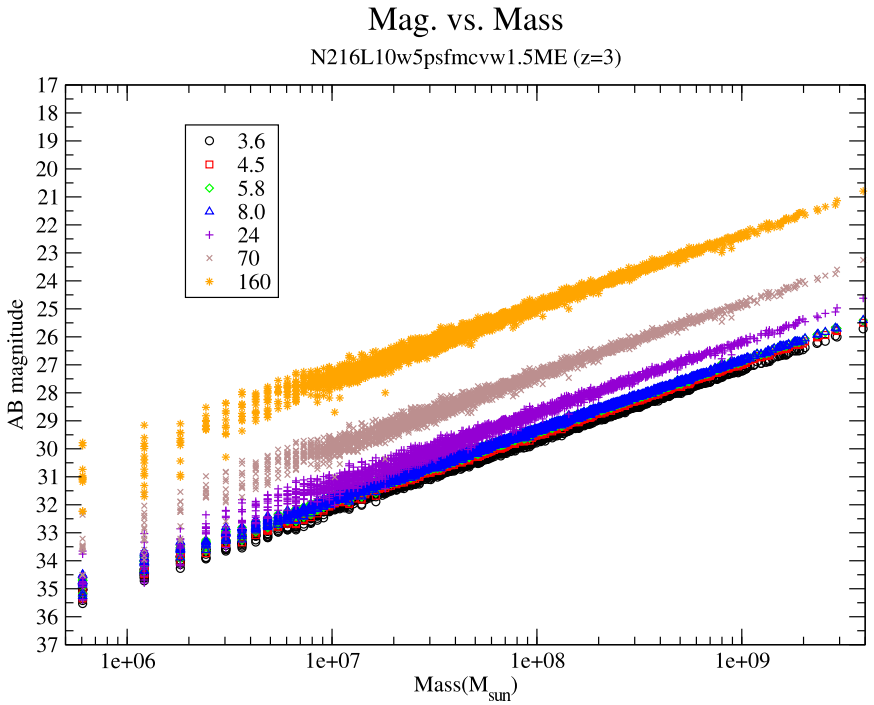

Figure 15 The galaxy mass with respect to AB magnitude. Each color represents IR wavelengths (in μm) of *Spitzer*

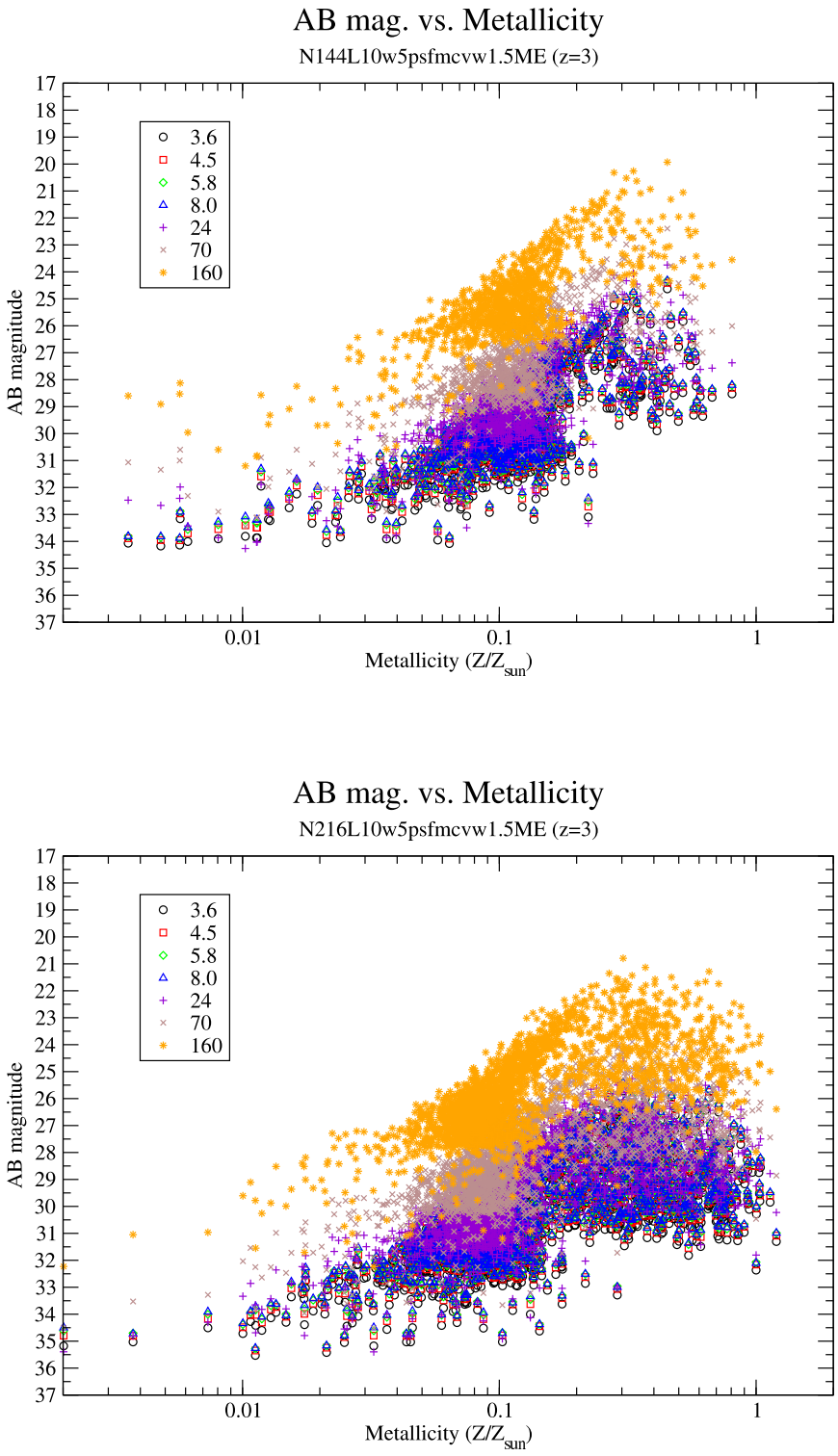

Figure 16 The galaxy metallicty with respect to AB magnitude. Each color represents IR wavelengths (in μm) of *Spitzer*

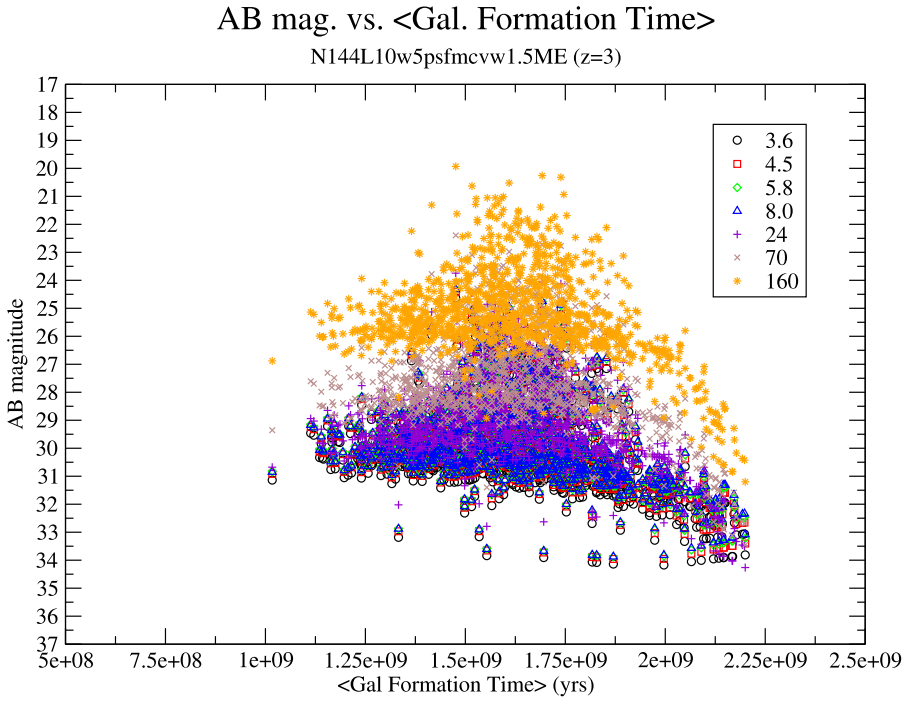

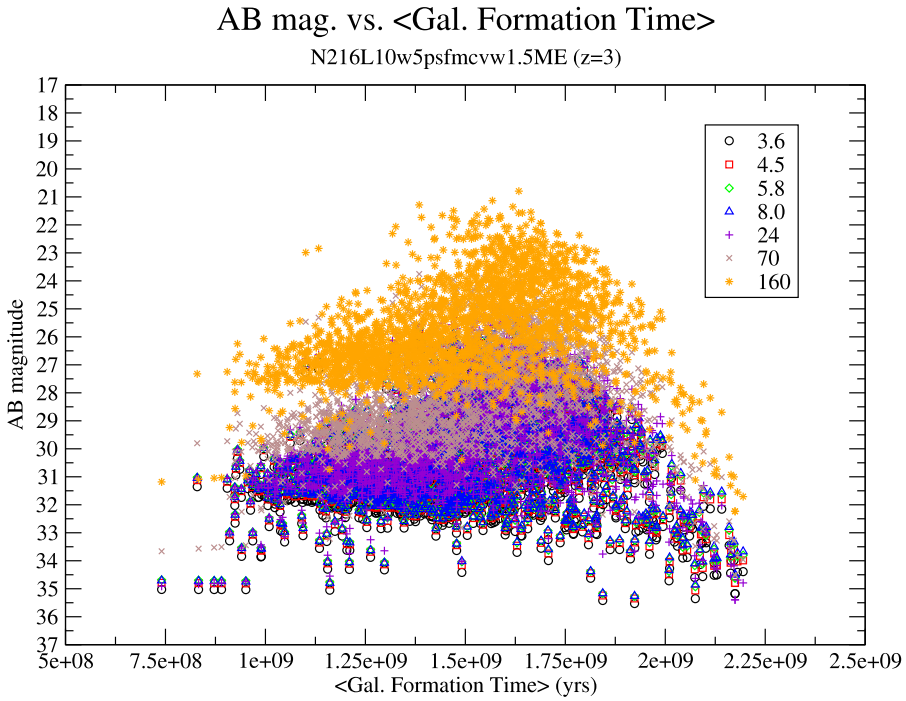

Figure 17 The galaxy average formation time with respect to AB magnitude. Each color represents IR wavelengths (in μm) of *Spitzer*

our limit, but it might fall within their error if our simulation can resolve the higher luminous galaxies.

Finally, we expend our comparison up to $z \sim 2.5$. At high redshift (Figure 19) only available data come from computed luminosities from GOODS+VVDS-SWIRE sample by Rodighiero et al. (2009). The data published in their paper from first time attempt under their sample and for both 8 μm and 24 μm their results support our method by having pretty good agreement within the most data points except the less luminous galaxies. This difference presumably results from some combination of sample size and detection limit of less luminous galaxies because it consistently shows that their values are lesser than our data at the lower L.

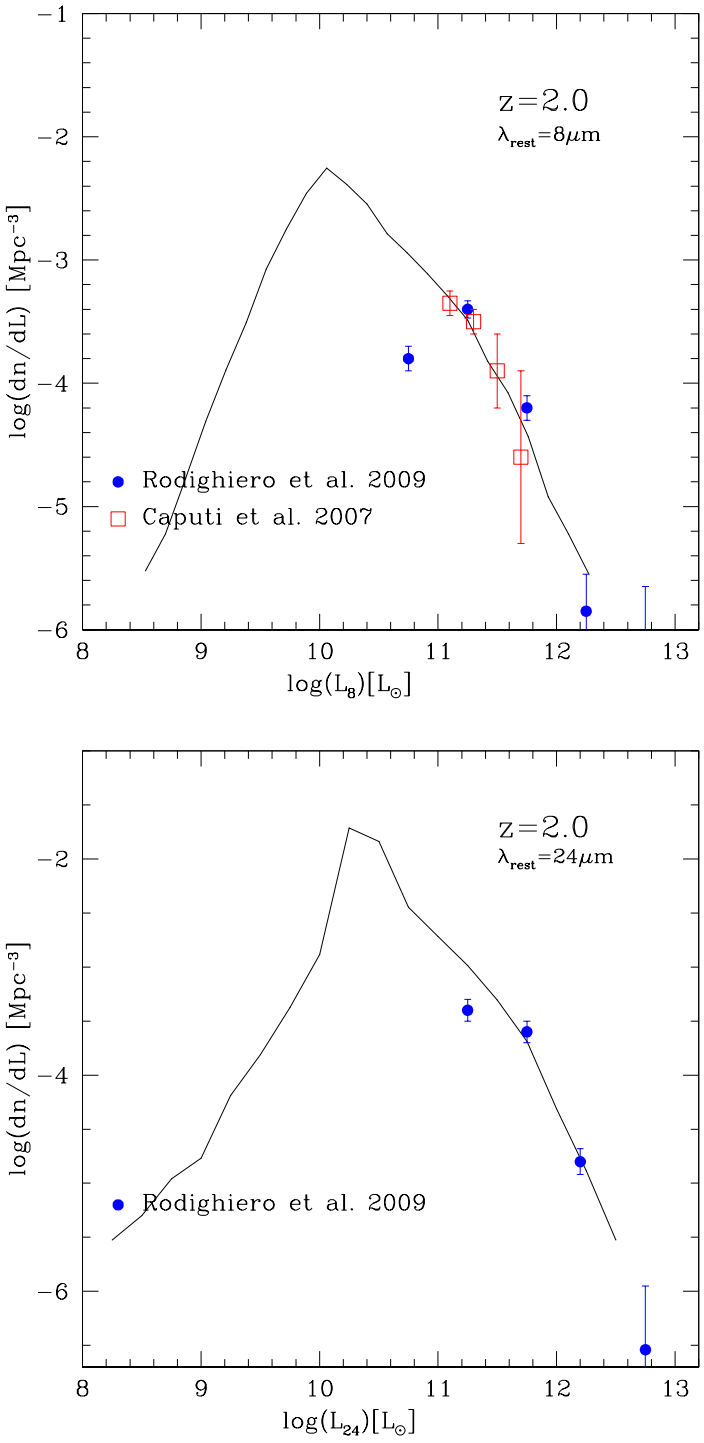

Figure 18 LFs at z=2.0 for N400 simulation. First and second panel show 8 μm and 24 μm, respectively. Our results are shown by the black solid line. The blue filled circles with error bars are the sampling data from Rodighiero et al. (2009). The observational data from Caputi et al. (2007) are shown in the opened square with the error bars.

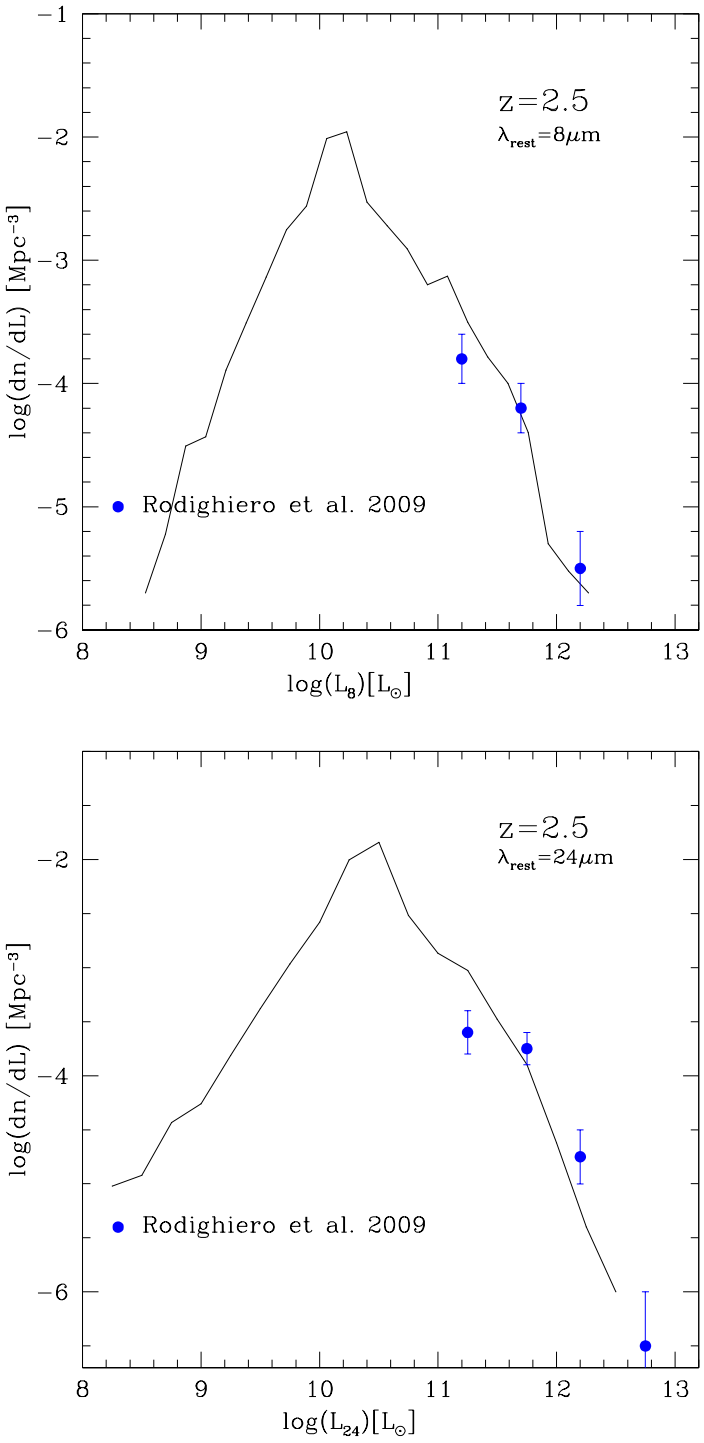

Figure 19 LFs at z=2.5 for N400 simulation. First and second panel show 8 μm and 24 μm, respectively. Our results are shown by the black solid line. The blue filled circles with error bars are the sampling data from Rodighiero et al. (2009)

CHAPTER 13

PART II: SUMMARY AND CONCLUSION

This work makes a first effort to compute and predict the dust distribution at different time epochs at 7 IR *Spitzer* bands (IRAC and MIPS) using cosmological SPH simulations. We calculate the SEDs with the GRASIL code in multiple metallicities (Z=0.0001, 0.0004, 0.004, 0.008, 0.02, 0.05, and 0.1) and time range. GRASIL computes the luminosities of the stellar population in galaxies and the reprocessed radiation by dust including radiative transfer through a two-phase dust medium and calculates the distribution of grain temperatures in each galaxy based on a balance between heating and cooling.

We calculate the AB magnitude from L_λ based on Equation 3, which we convert from Equation 2 (Fukugita et al., 1996). We observe that AB magnitude of the N144 simulation has slightly higher value than N216 in all seven wavelengths, and the two of MIPS wavelengths (70 μm and 160 μm) show noticeably higher magnitude than other wavelengths. Using the AB magnitude information, we plot the mass, metallicity, and average formation time. They all show the same trend that the average AB magnitude of the N144 simulation is higher than the N216 simulation. Due to the longer collapsing time-scale (longer than 1 Gyr), SP Clusters in the N144 simulation are occupied with the younger galaxies with the metallicty less than $Z_\odot$=0.02.

For the galaxy LF, we start with the different simulation (400^3 particle numbers with 100 Mpc h^{-1} box) snapshot. We calculate rest-frame LFs at two wavelength bands (8 μm and 24 μm) and two time epochs (z=2.0 and 2.5) for comparison to the observational and sampling data. There was a slight disagreement especially at lower luminosity with Rodighiero et al. (2009), but it might be caused by their sampling limit from GOODS+VVDS-SWIRE data. Beside of the lower end, at both wavelengths and time epochs, we find pretty good agreement between our GAD-

GET+GRASIL simulations and previous measurements (Caputi et al., 2007) and sampling data (Rodighiero et al., 2009).

Our GADGET+GRASIL code can produce reliable results (e.g. SEDs and LFs) comparable to the real and sampling data. These preliminary results are encouraging to explain the IR properties of high redshift galaxies under the framework of ΛCDM model. This successful outcome can be extended to the further investigations such as how our method is sensitive to the choice of different IMFs (we use Salpeter profile) and how reliable at different time epochs and different wavelengths. In addition to LFs, we can start our comparison against *Spitzer* data with the galaxy number counts under the four IRAC and MIPS bands.

REFERENCES

Adelberger K. L., Steidel C. C., Giavalisco M., Dickinson M.,Pettini M., Kellogg M., 1998, ApJ, 505, 18

Adelberger K. L., Steidel C. C., Pettini M., Shapley A. E., Reddy N. A., Erb D. K., 2005, ApJ, 619, 697

Adelberger K. L., Steidel C. C., Shapley A. E., Pettini M., 2003, ApJ, 584, 45

Avni, Y. 1976, ApJ, 210, 642

Babbedge, T. S. R., et al. 2006, MNRAS, 370, 1159

Bardeen J. M., Bond J. R., Kaiser N., Szalay A. S., 1986, ApJ, 304, 15

Barnes, J., & Hut, P. 1986, Nat, 324, 446

Baugh C. M., Cole S., Frenk C. S., Lacey C. G., 1998, ApJ, 498, 504

Bertelli, G., Bressan, A., Chiosi, C., Fagotto, F., & Nasi, E. 1994, A&AS, 106, 275

Bouche N., Gardner J. P., Weinberg D. H., Davé R., Lowenthal J. D., 2005, ApJ, 628, 89

Bouche N., Lowenthal J. D., 2004, ApJ, 609, 513

Bressan, A., Chiosi, C., & Fagotto, F. 1994, ApJS, 94, 63

Bressan, A., Silva, L., & Granato, G. L. 2002, A&A, 392, 377

Caputi, K. I., et al. 2007, ApJ, 660, 97

Choi, J.-H., & Nagamine, K. 2009, MNRAS, 393, 1595

Choi, J.-H., & Nagamine, K. 2009, arXiv:0909.5425

Choi, J.-H., & Nagamine, K. 2010, arXiv:1001.3525

Cooke J., Wolfe A. M., Gawiser E., Prochaska J. X., 2006a, ApJL, 636, L9

Cooke J., Wolfe A. M., Gawiser E., Prochaska J. X., 2006b, ApJ, 652, 994

Davé R., Hernquist L., Katz N., Weinberg D. H., 1999, ApJ, 511, 521

Elbaz, D., et al. 1999, A&A, 351, L37

Elbaz, D., Cesarsky, C. J., Chanial, P., Aussel, H., Franceschini, A., Fadda, D., & Chary, R. R. 2002, A&A, 384, 848

Fang, F., Shupe, D. L., Xu, C., & Hacking, P. B. 1998, ApJ, 500, 693

Fukugita, M., Ichikawa, T., Gunn, J. E., Doi, M., Shimasaku, K., & Schneider, D. P. 1996, AJ, 111, 1748

Gawiser E., Francke H., Lai K., Schawinski K., Gronwall C., Ciardullo R., Quadri R., Orsi A., et al., 2007, ArXiv e-prints, 710

Gawiser E., Wolfe A. M., Prochaska J. X., Lanzetta K. M., Yahata N., Quirrenbach A., 2001, ApJ, 562, 628

Giavalisco M., Steidel C. C., Adelberger K. L., Dickinson M. E., Pettini M., Kellogg M., 1998, ApJ, 503, 543

Haardt F., Madau P., 1996, ApJ, 461, 20

Hacking, P., Houck, J. R., & Condon, J. J. 1987, ApJL, 316, L15

Hauser, M. G., et al. 1998, ApJ, 508, 25

Hernquist L., Katz N., Weinberg D. H., Miralda-Escude, J. 1996, ApJ, 457, L51

Hockney, R. W., & Eastwood, J. W. 1988, Bristol: Hilger, 1988,

Kaiser N., 1984, ApJL, 284, L9

Katz N., Hernquist L., Weinberg D. H., 1999, ApJ, 523, 463

Katz N., Weinberg D. H., Hernquist L., 1996, ApJS, 105, 19

Katz N., Weinberg D. H., Hernquist L., Miralda-Escude, J. 1996, ApJ, 457, L57

Kauffmann G., Colberg J. M., Diaferio A., White S. D. M., 1999, MNRAS, 303, 188

Landy S. D., Szalay A. S., 1993, ApJ, 412, 64

Lee K.-S., Giavalisco M., Gnedin O. Y., Somerville R. S., Ferguson H. C., Dickinson M., Ouchi M., 2006, ApJ, 642, 63

Le Floc'h, E., et al. 2005, ApJ, 632, 169

Lowenthal J. D., Koo D. C., Guzman R., Gallego J., Phillips A. C., Faber S. M., Vogt N. P., Illingworth G. D., et al., 1997, ApJ, 481, 673

Marigo, P., Girardi, L., Bressan, A., Groenewegen, M. A. T., Silva, L., & Granato, G. L. 2008, A&A, 482, 883

Mo H. J., Fukugita M., 1996, ApJ, 467, L9

Mo H. J., Mao S., White S. D. M., 1999, MNRAS, 304, 175

Mo H. J., White S. D. M., 2002, MNRAS, 336, 112

Nagamine K., Ouchi M., Springel V., Hernquist L., 2008, ArXiv e-prints, 802

Nagamine K., Springel V., Hernquist L., 2004a, MNRAS, 348, 421

Nagamine K., Springel V., Hernquist L., 2004b, MNRAS, 348, 435

Nagamine K., Springel V., Hernquist L., Machacek M., 2004, MNRAS, 350, 385

Nagamine, K., Cen, R., Hernquist, L., Ostriker, J. P., & Springel, V. 2005, ApJ, 627, 608

Nagamine, K., Cen, R., Hernquist, L., Ostriker, J. P., & Springel, V. 2005, ApJ, 618, 23

Nagamine K., Wolfe A. M., Hernquist L., Springel V., 2007, ApJ, 660, 945

Oke, J. B., & Gunn, J. E. 1983, ApJ, 266, 713

Papovich C., Dickinson M., Ferguson H. C., 2001, ApJ, 559, 620

Peebles P. J. E., 1980, The large-scale structure of the universe. Research supported by the National Science Foundation. Princeton, N.J., Princeton University Press, 1980. 435 p.

Pérez-González, P. G., et al. 2005, ApJ, 630, 82

Pontzen A., Governato F., Pettini M., Booth C. M., Stinson G., Wadsley J., Brooks A., Quinn T., Haehnelt M., 2008, ArXiv e-prints, 804

Press W. H., Teukolsky S. A., Vetterling W. T., Flannery B. P., 1992, Numerical recipes in C. The art of scientific computing. Cambridge: University Press, —c1992, 2nd ed.

Puget, J. L., et al. 1999, A&A, 345, 29

Rodighiero, G., et al. 2009, arXiv:0910.5649

Saunders, W., Rowan-Robinson, M., Lawrence, A., Efstathiou, G., Kaiser, N., Ellis, R. S., & Frenk, C. S. 1990, MNRAS, 242, 318

Sawicki M. J., Yee H. K. C., 1998, AJ, 115, 1329

Shapley A. E., Steidel C. C., Adelberger K. L., Dickinson M., Giavalisco M., Pettini M., 2001, ApJ, 562, 95

Sheth R. K., Tormen G., 1999, MNRAS, 308, 119

Shupe, D. L., Fang, F., Hacking, P. B., & Huchra, J. P. 1998, ApJ, 501, 597

Silva, L., Granato, G. L., Bressan, A., & Danese, L. 1998, ApJ, 509, 103

Somerville R. S., Primack J. R., Faber S. M., 2001, MNRAS, 320, 504

Springel V., 2005, MNRAS, 364, 1105

Springel V., Hernquist L., 2002, MNRAS, 333, 649

Springel V., Hernquist L., 2003a, MNRAS, 339, 289

Springel V., Hernquist L., 2003b, MNRAS, 339, 312

Steidel C. C., Adelberger K. L., Dickinson M., Giavalisco M., Pettini M., Kellogg M., 1998, ApJ, 492, 428

Steidel C. C., Adelberger K. L., Giavalisco M., Dickinson M., Pettini M., 1999, ApJ, 519, 1

Storrie-Lombardi L. J., Wolfe A. M., 2000, ApJ, 543, 552

Weatherley S. J., Warren S. J., 2003, MNRAS, 345, L29

Wolfe A. M., Prochaska J. X., Gawiser E., 2003, ApJ, 593, 215

Wolfe A. M., Turnshek D. A., Smith H. E., Cohen R. D., 1986, ApJS, 61, 249

VITA

Graduate College
University of Nevada, Las Vegas

Tae Song Lee

Local Address:
4200 Paradise Rd. Apt. 2078
Las Vegas, NV 89169

Degree:
Bachelor of Science, Physics, 1998
California State University, Northridge, CA

Master of Science, Physics, 2007
University of Nevada, Las Vegas, NV

Dissertation Title: DLA-LBG Cross-correlation and Basic Properties of Infrared Galaxies in Cosmological Simulations

Dissertation Committee:
Chairperson, Dr. Kentaro Nagamine, Ph.D.
Committee Member, Dr. Bing Zhang, Ph.D.
Committee Member, Dr. Daniel Proga, Ph.D.
Graduate Faculty Representative, Dr. Balakrishnan Naduvalath, Ph.D.